UNIVERSITÀ DEGLI STUDI DI PADOVA

UNIVERSITA' DEGLI STUDI DI PADOVA

Department of Industrial Engineering DII

MASTER OF SCIENCE IN MECHANICAL ENGINEERING

HIGH FIDELITY SIMULATIONS OF THE SUPERSONIC WAKE OF A REENTRY VEHICLE

Thesis advisor: Prof. Francesco Picano

Thesis co-advisors: Ing. Michele Cogo,

Ing. Luca Placco

Candidate: Umberto Baù

Matriculation number: 1237208

Academic Year 2021/2022

SOMMARIO

Lo scopo di questo lavoro consiste nel riprodurre tramite simulazioni numeriche l'evoluzione temporale della scia prodotta dalla capsula ExoMars nella fase descent della sequenza EDL (Entry-Descent-Landing) eseguita su Marte. Come si può leggere nel documento "EXOMARS 2016 – Schiaparelli Anomaly Inquiry" [4], elaborato per investigare sul fallimento della missione ExoMars 2016, in seguito all'apertura del paracadute si sono manifestate oscillazioni laterali della capsula non previste. Il paracadute ha funzionato, ma il suo comportamento a Mach 2 non era stato sufficientemente studiato. Tali oscillazioni hanno corrotto le misurazioni di assetto e altitudine e portato allo schianto della sonda Schiaparelli sulla superficie di Marte. Numerosi studi [5,6,7,8] riconducono l'esibirsi di tali instabilità all'interazione tra la scia turbolenta prodotta dalla capsula e l'onda d'urto che si forma di fronte al paracadute. La tecnica utilizzata in questo lavoro è la tecnica implicit LES (Large-Eddy Simulations). Tale approccio consiste nel simulare solamente i vortici più grandi di un flusso turbolento e nel trattare l'effetto prodotto dai vortici più piccoli affidandosi alla dissipazione intrinseca degli schemi numerici adottati. In questo modo è possibile trattare i flussi ad elevato Reynolds e ricostruire fedelmente la regione turbolenta che si forma in scia ad una capsula in rientro atmosferico. Il solutore impiegato è STREAmS, un solutore validato su flussi canonici (canale supersonico, strato limite supersonico, interazione tra onda d'urto e strato limite), il quale implementa una formulazione ibrida tra schemi conservativi e ricostruzioni WENO. Tale strategia si rivela essere ottimale nel trattamento di campi fluidodinamici che presentano discontinuità e regioni turbolente. Il primo capitolo della tesi è rivolto a fornire il contesto delle analisi che sono state eseguite, parlando delle problematiche riscontrate durante la sequenza EDL della missione ExoMars 2016 e degli aspetti aerodinamici che caratterizzano l'interazione tra scia e paracadute. In seguito, il secondo capitolo espone i metodi numerici messi in gioco per trattare il flusso di scia. Infine, nel terzo capitolo vengono esposti i risultati delle simulazioni lanciate per diversi angoli di attacco della capsula. Con i risultati ottenuti si vuole valutare il comportamento della scia, valutare l'efficacia della metodologia implementata e fornire quindi supporto ad ulteriori studi volti a comprendere gli aspetti aerodinamici coinvolti nelle fasi di rientro atmosferico.

CONTENTS

1. INTRODUCTION: Failure of Schiaparelli 1

1.1 Supersonic parachutes aerodynamics 4
1.2 Wake flow 8
1.3 Turbulence 9

2. METHODOLOGY. 13

2.1 Mathematical model 14
2.2 Numerical treatment. 16
2.3 Comparison between DNS, RANS, and LES. 19
2.3.1 Direct Numerical Simulations (DNS) 19
2.3.2 Reynolds-Average Navier-Stokes (RANS) 21
2.3.3 Large-Eddy Simulations (LES) 23
2.4 Immersed Boundary Method. 25
2.4.1 The Direct Forcing Method 27
2.4.2 The Ghost Point Forcing Method 28

3. RESULTS 31

3.1 Flow field 32
3.2 Aerodynamic coefficients 38
3.3 Wake profiles 40

4. CONCLUSIONS 43

CHAPTER 1

INTRODUCTION: failure of Schiaparelli

"Establishing if life is ever existed on Mars is one of the outstanding scientific questions of our time. To address this important goal, the European Space Agency (ESA) has established the ExoMars programme to investigate the Martian environment and to demonstrate new technologies paving the way for a future Mars sample return mission in the 2020's". These words, currently reported on the ESA official website [1], present ongoing exploration of the Red Planet wich is being conducted by the agency. It can be read that the ExoMars programme consists of two missions, both in cooperation with Roscosmos, conceived to ship to Mars:

- the Trace Gas Orbiter (TGO) coupled to the Entry, Descent, and landing Module (EDM), known as Schiaparelli, launched on 14 March 2016.
- the Rosalind Franklin rover with a launch date of 2022.

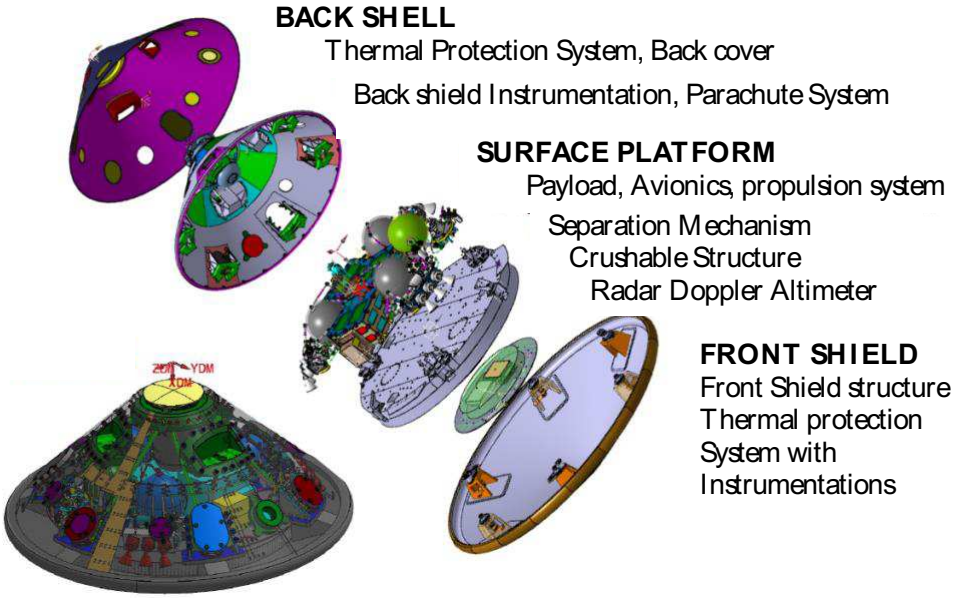

Figure 1.1: ExoMars EDM major components [3].

The TGO carries scientific instruments to detect methane or other atmospheric trace gases (water vapor, nitrogen oxides, acetylene) and orbits approximately at 400 km of altitude searching for signatures of biological or geological processes [2]. Schiaparelli is shown in figure 1.1 and was conceived

as a demonstration vehicle to validate the Entry, Descent, and Landing (EDL) sequence on Mars in preparation for the next mission [3]:

- Entry: after entering the atmosphere, Schiaparelli decelerates because of atmospheric drag, and it's protected from intense aerodynamic heating by a front heat shield. At an altitude of about 11 km the parachute is deployed while the vehicle is traveling at 1700 km/h.
- Descent: the module firstly releases the front shield at an altitude of about 7 km, turn on the Radar Doppler Altimeter (RDA) to measure the distance to the ground and its velocity relative to the surface, then releases the rear cover and parachute system at an altitude of about 1.2 km.
- Landing: at an altitude of about 1.1 km thrusters are ignited to reduce vehicle speed from 250 km/h to 4 km/h and then complete the touchdown

Diameter	2.40 m (with front shield) 1.65 m (without front shield)
Height	1.80 m
Mass	577 kg (wet)
Parachute	Disk-Gap-Band canopy, 12 m diameter

Table 1.1: main technical characteristics of Schiaparelli [3].

On 19 October 2016, Schiaparelli separated from the TGO, entered Mars's atmosphere but failed the EDL sequence and crashed on the surface. Investigations were conducted and on 24 May 2017 ESA published an inquiry. It concluded that conflicting information in the onboard computer caused a premature ending of the descent phase. As reported on the document "EXOMARS 2016 – Schiaparelli Anomaly Inquiry" [4] the deployment and inflation of the parachute caused unexpected lateral angular oscillations of the capsule. This resulted in a saturation (the expected measurement range is exceeded) of the Inertial Measurement Unit (IMU), corrupting the attitude estimation and determining:

1. Early release of the back shell and parachute system.
2. Brief firing of the thrusters for only 3 sec instead of 30 sec.
3. Activation of the onground system as if Schiaparelli had landed (the vehicle was instead in free fall from an altitude of about 3.7 km).

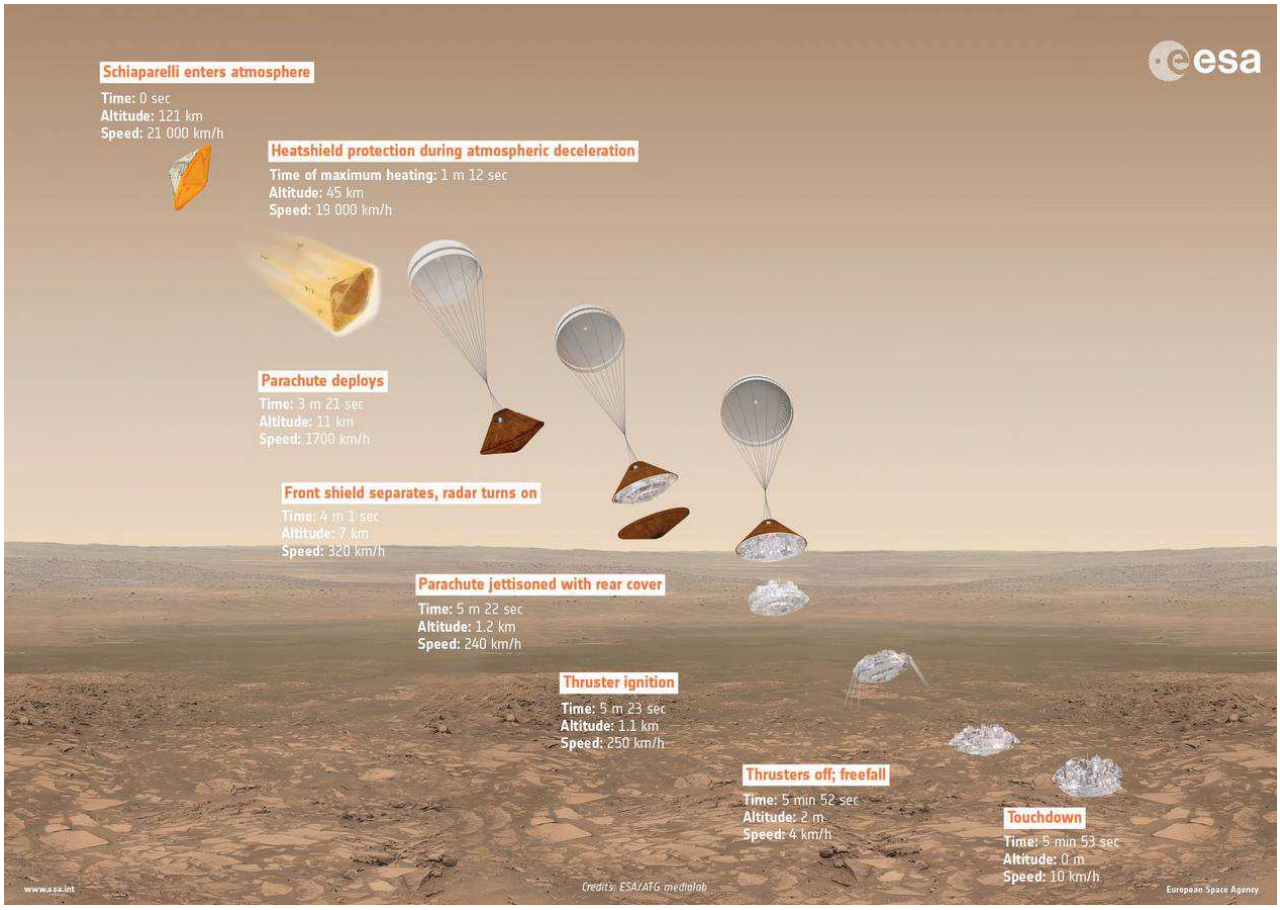

Figure 1.2: Schiaparelli's nominal EDL sequence [3].

David Parker, director of human and robotic exploration, explains "There were clearly a number of areas that should have been given more attention in the preparation, validation and verification of the entry, descent and landing system". "Interestingly, had the saturation not occurred and the final stages of landing had been successful, we probably would not have identified the other weak spots that contributed to the mishap", notes Jan Woerner, ESA's Director General. "As a direct result of this inquiry we have discovered the areas that require particular attention that will benefit the 2020 mission". The first recommendation stated in the section "Identified Weaknesses and Areas for Improvements" of the inquiry [4] lists the following areas as to be improved for the multi-body modelling employed for the parachute inflation simulations:

- Riser angle at inflation.
- Asymmetric inflation.
- Area oscillations as a function of Mach number.
- Lateral instability as a function of Mach number.

1.1 Supersonic parachutes aerodynamics

Supersonic parachutes are textile devices designed to be deployed in supersonic regimes and to provide aerodynamic drag for atmospheric entry vehicles deceleration. Supersonic parachutes have been proven to provide [5]:

- Deceleration from supersonic flight to subsonic flight.
- Proper descent rates for Mars's low-density, thin atmosphere thanks to high ratios between drag and parachute mass.
- Limited canopy oscillations when deployed in unsteady conditions characterizing the wake produced by the capsule.

There are different models of supersonic parachutes based on the conditions in wich it is intended to be deployed. Table 1.2 shows a list of past and present robotic exploration missions and relative models adopted.

Mission	Entry Year	Agency/ Country	Destination	Parachute type	Nominal Diameter(m) or Area(m^2)	Deployment Mach number	Deployment method	EDL Comments
Viking 1&2	1976	NASA	Mars	DGB	16.2	2.1	Mortar	Successful
Pioneer Venus	1978	NASA	Venus	1) Ribless Guide Surface	1) 0.76	1) 0.8	1) Mortar	Successful
				2) Conical Ribbon	2) 4.94	2) 0.8	2) Pilot Parachute	
Galileo	1995	NASA	Jupiter	1) Conical Ribbon	1) 1.14	1) 0.95	1) Mortar	Successful
				2) Conical Ribbon	2) 3.8	2) 0.95	2) Pilot Parachute	
MPF	1997	NASA	Mars	DGB	12.7	1.71	Mortar	Successful
MPL	1999	NASA	Mars	DGB	12.7	1.85	Mortar	Failure
Beagle 2	2003	ESA	Mars	1) DGB	1) 3.2	1) 1.5	1) Mortar	Lander lost on arrival
				2) Ringsail	2) 10.0	2) 0.4–0.6	2) Pilot Parachute	
MER A&B	2004	NASA	Mars	DGB	14.1	1.8 &1.9	Mortar	Successful
Huygens	2004	ESA	Titan	1) DGB	1) 2.6	1) 1.47	1) Mortar	Successful
				2) DGB	2) 8.3	2) 1.36	2) Pilot Parachute	
				3) DGB	3) 3.0	3) 0.15	3) Pilot Parachute	
Genesis	2004	NASA	Earth[1]	1) DGB	1) 2.03	1) 1.8	1) Mortar	DGB Parachute failed to deploy
				2) Parafoil	2) 325	2) subsonic	2) Pilot Parachute	
Stardust	2006	NASA	Earth[2]	1) DGB	1) 0.8	1) 1.4	1) Mortar	Successful
				2) Triconical	2) 7.3	2) 0.15	2) Pilot Parachute	
Phoenix	2008	NASA	Mars	DGB	11.7	1.74	Mortar	Successful
MSL	2010	NASA	Mars	DGB	21.5	1.75	Mortar	Successful
ExoMars	2016	ESA/Russia	Mars	DGB	12.0	1.8–2.2	Mortar	Lander lost on arrival
InSight	2018	NASA	Mars	DGB	11.8	1.49	Mortar	Successful
Tianwen-1	2021	CNSA	Mars	DGB	200	1.8	Mortar	Successful

Table 1.2: past and present robotic exploration missions with supersonic parachutes [5].

Figure 1.3: Schiaparelli DGB parachute during testing [3].

Schiaparelli used a Disk-Gap-Band (DGB) parachute, the model of supersonic parachute used for EDL sequences wich turned out to have been completed successfully like Viking 1 (1976) and Viking 2 (1978) or, more recently, Huygens (2004) and Stardust (2006). The canopy, shown in figure 1.3, had a nominal diameter of 12 meters and was made from nylon fabric, while the lines were made from Kevlar [3]. The DGB parachute is designed to be deployed above Mach 1.5 and is observed to exhibit better drag and stability performances than other supersonic parachute models [5].

Supersonic parachutes deployment and inflation can suffer from problems related to instability phenomena. Several studies observed complex interdependent phenomena around the two-body system consisting of the capsule and the canopy. These include interactions between the wake produced by the capsule and the shock wave that originates in front of the canopy. Figure 1.4 shows unsteadiness of the flow field around a DGB parachute placed in wake of a Viking capsule.

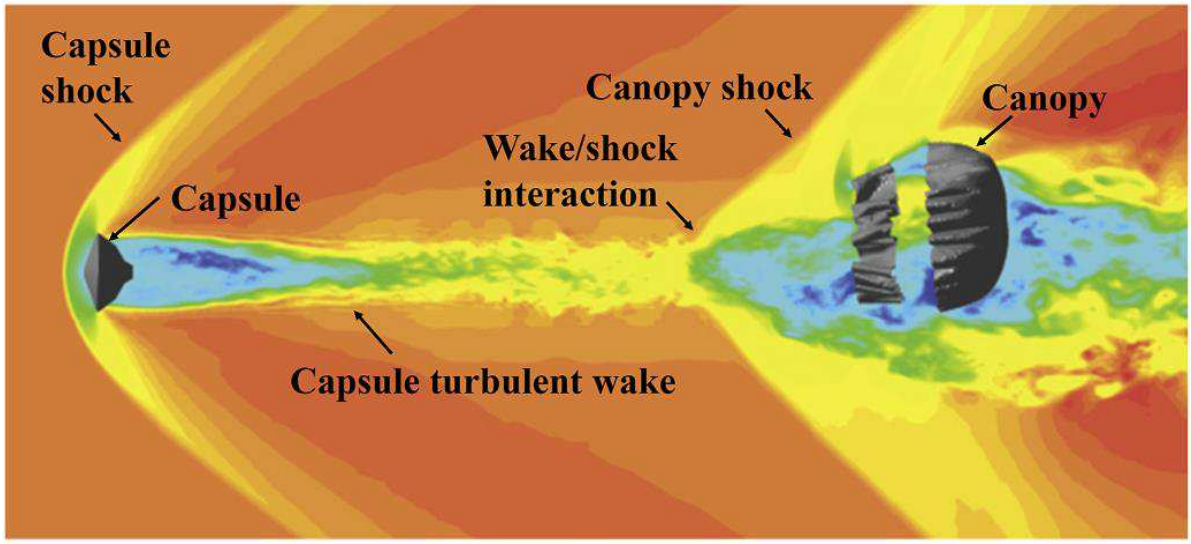

Figure 1.4: unsteady flow fields around a DGB parachute placed behind a Viking capsule [5].

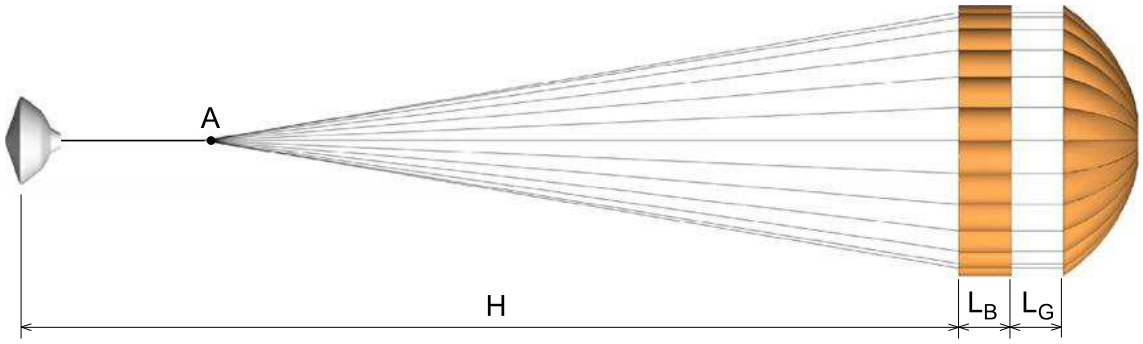

Figure 1.5: two-body system consisting of a Viking capsule and DGB parachute [5].

The main parameters used to evaluate the aerodynamic behavior of supersonic parachutes are drag coefficient and stability [5]. First studies on the aerodynamical behavior of parachutes placed in a supersonic flow were conducted by Meyer [6] and Maynard [7]. The wake produced by the capsule was observed to interact with the bow shock ahead of the parachute, causing large pressure fluctuations inside the canopy. Large canopy deformations, including periodic collapse and re-inflation events, called cyclical 'area oscillations' or 'canopy breathing instabilities', occurred leading to poor drag and stability performances. Large-eddy simulations were carried out by K. Karagiozis et al. [8] to reproduce the canopy area oscillations wich manifests usually for a capsule-parachute systems above Mach 1.5. The system being investigated is shown in figure 1.5 and consists of a Viking capsule coupled to a DGB parachute. The calculated drag was compared to experimental data and was observed to decrease with increasing Mach number.

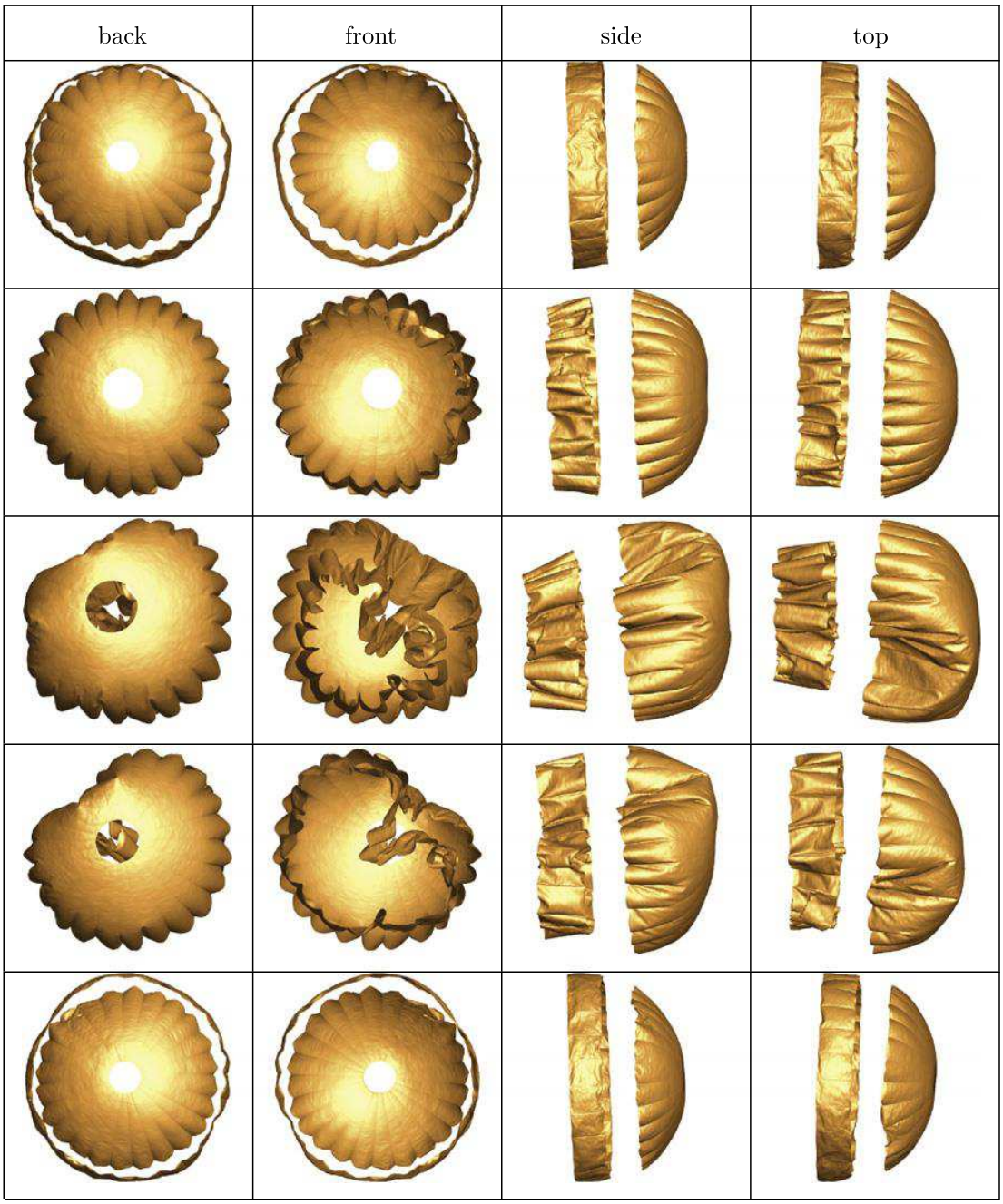

Fig. 1.6: four views of a complete canopy breathing cycle from a simulation at Mach 2 [8].

A large amount of data from wind tunnel experiments, flight tests, and numerical simulations was collected by X. Xue and C. Wen [5] wich provided a systematic review of the unsteady aerodynamics of supersonic parachutes:

- Parachutes manifest canopy breathing in a supersonic regime leading to drag decreases.
- Area oscillations are triggered by the fluctuations characterizing the turbulent wake and sustained by the interaction between the wake and the canopy bow shock.

- The key parameters affecting parachutes performances are the Mach number, canopy-capsule trailing distance, canopy-capsule diameter ratio, canopy configuration and canopy geometric porosity.
- Reynolds number, dynamic pressure and material properties have a limited effect on parachutes performances.
- The DGB parachute exhibit better performances than other model of supersonic parachutes.
- The angle of attack of the capsule or the canopy produces asymmetrical flow fields around the parachute wich intensifies lateral oscillations.

1.2 Wake flow

The purpose of this work is to reproduce the behavior of the wake produced by the ExoMars capsule during the descent phase of the EDL sequence performed on Mars. Numerical simulations are performed following an implicit large-eddy approach to obtain a precise time-evolution development of the supersonic, turbulent wake flow. Different capsule angles of attack are investigated to:

- Evaluate the wake and flow field patterns for different attitudes.
- Evaluate the capsule stability through aerodynamic coefficients data.
- Evaluate the wake trailing influence through wake properties profiles at different trailing distances.

The supersonic capsule flight is an important fluid dynamic problem wich has applications for atmospheric entry vehicles. The flow field wich establishes around an entry capsule in a supersonic regime exhibit typical features [9,10]:

- Development of a bow shock ahead of the capsule because of flight speeds above the speed of sound. The strong compression induced by the bow shock results in temperature, density, and pressure discontinuities wich reach their maximum values at the stagnation point.
- Development of a near wake recirculation region. Downstream the capsule's shoulder, the detached flow, sundered from the recirculation region by a shear layer (dividing streamline), accelerates resulting in an expansion fan. The near wake maintains a laminar nature at some Reynolds and Mach ranges [9].

- Development of a recompression shock (trailing shock) behind the capsule resulting from the reattachment of the supersonic detached flow.
- Development of a turbulent wake region characterized by a wide spectrum of vortical structures.

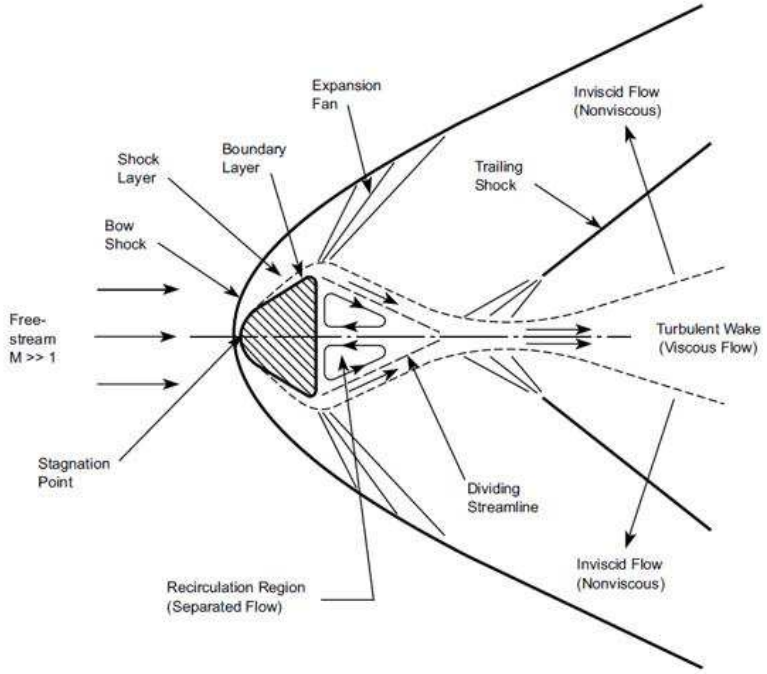

Figure 1.7: sketch of the flow field configuration for a capsule supersonic flight [9].

This first chapter introduces the framework of this survey and discuss about the aerodynamical aspects we want to investigate. The second chapter expose the implemented methodology for treating the wake flow and finally, in the conclusion chapter, are exposed the results wich will allow us to evaluate both the wake characteristics and the effectiveness of the exploited procedure.

1.3 Turbulence

In fluid dynamics, turbulence [11] is a phenomenon wich manifests itself through chaotic fluctuations of the flow properties. The chaotic behavior of turbulent flows comes from the action of unsteady vortices intertwined with each other. The onset of this phenomenon is regulated by the Reynolds number wich represents the ratio between inertial forces and viscous forces and it is defined as:

$$Re_0 = \frac{U_0\, l_0}{\nu} \tag{1.1}$$

where U_0 and l_0 are the characteristic velocity and the characteristic length, respectively, of the fluid system, while ν is the kinematic viscosity of the fluid. For an entry capsule U_0 represents the flight speed, l_0 represents the capsule's shoulder diameter while ν represents the kinematic viscosity of the atmosphere. It can be proven with simple experiments [12] that turbulence occurs when the Reynolds number tends to become much bigger than the unit, i.e., when $Re_0 \gg 1$. From that, we know that flow instabilities generate and sustain their self because molecular viscosity is unable to damp velocity gradients. The descent phase of an atmospheric entry on Mars is characterized by high Reynolds numbers (AMELIA [31]), consequently the wake produced by the capsule is turbulent. Turbulence has strong implications on the wake flow's characteristics:

- It breaks symmetries imposed by the boundary conditions, so the wake flow is asymmetrical and unsteady even if the capsule is axysimmetric and the flight speed is constant.
- It gives rise to a wide, continuous spectrum of vortical structures leading to a wake region with a multi – scale structure.

Vortical structures, also called eddies, are portions of the fluid wich moves with spatial regularity. To a vortical structure we can associate a characteristic length (scale) l and a characteristic velocity u_l. Turbulent motions range in size from the characteristic sizes of the fluid system to much smaller scales wich become progressively smaller as the Reynolds number increases. Richardson [13] firstly introduced the energy cascade concept: the kinetic energy of the flow enters at the largest scales of motion and is transferred through inertial processes to the smallest scales of motion where is dissipated by viscous action. The size of the smallest eddies (Kolmogorov' scale) that are responsible of for dissipating the kinetic energy into thermic energy was investigated by Kolmogorov in its K41 theory. The Kolmogorov's K41 theory [14] is founded on three main hypotheses:

- Microscopically, turbulent flows are homogeneous and isotropic, the statistics of the small-scale turbulent motions ($l \ll l_0$) are universal.
- The statistics of the smallest scales ($l \sim \eta$), where energy viscous dissipation occurs, depend on energy dissipation ε and kinematic viscosity ν.
- The statistics of the intermediate scales ($\eta \ll l \ll l_0$), where energy inertial transferring occurs, depend on energy dissipation ε.

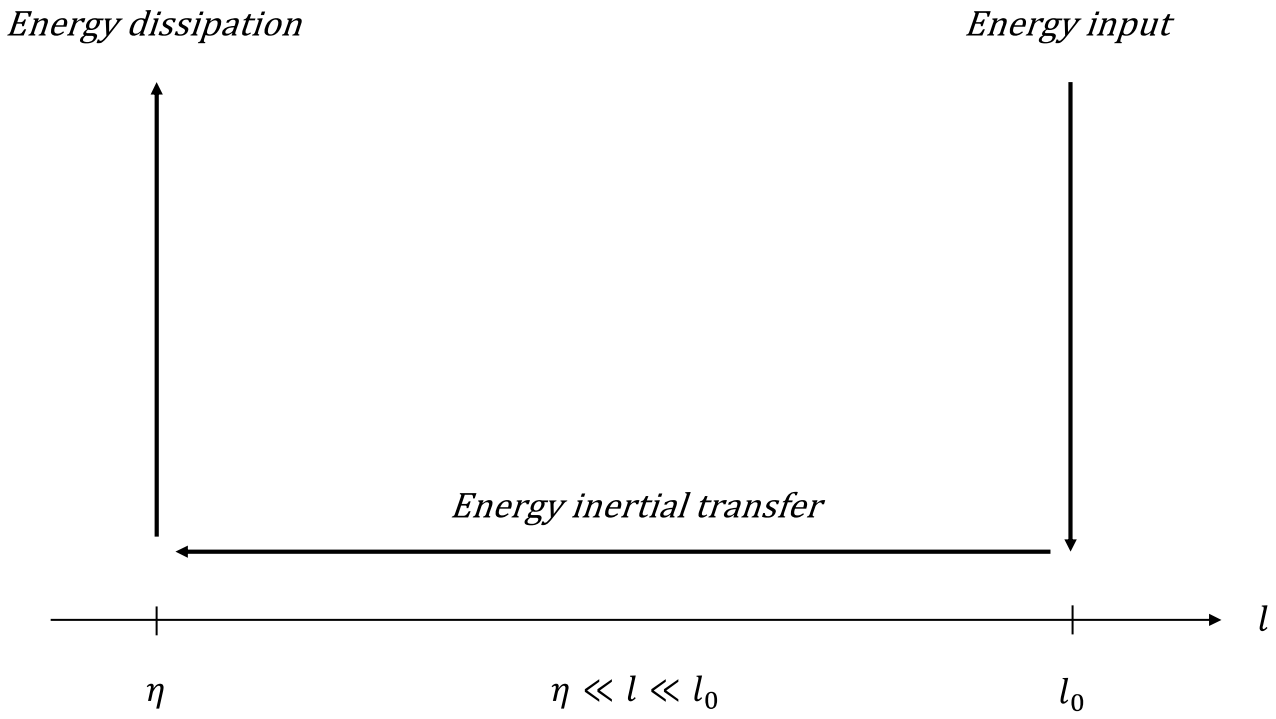

Figure 1.8: scheme of the kinetic energy dissipation occurring in a turbulent flow.

We can define a Reynolds number related to a turbulent motion of scale l:

$$Re_l = \frac{u_l l}{\nu} \tag{1.2}$$

According to Richardson phenomenology [13]:

- $Re_l \gg 1$ for scales where inertial phenomena are preponderant: $l \sim l_0$ and $\eta \ll l \ll l_0$.
- $Re_l \sim 1$ for scales where viscous phenomena are preponderant: $l \sim \eta$.

One fundamental result of the K41 theory consists in the fact that the Kolmogorov's scale become smaller as the Reynolds number increase, expanding the spectrum of vortical structures [14]:

$$\frac{l_0}{\eta} = Re_0^{3/4} \tag{1.3}$$

CHAPTER 2

METHODOLOGY

This chapter presents the methodological structure wich the current fluid dynamical investigation is based on and expose the numerical methods that are implemented. The flow field that establishes around an entry capsule during the descent phase of the EDL sequence can be described by the Navier-Stokes systems of equations, a system of partial differential equations (PDE) wich derives from laws of mass, momentum, and energy conservation. This mathematical model can describe a wide variety of fluid systems but remaining within the continuum mechanic hypothesis. A fluid can be represented by a continuum if the mean free path of molecules, i.e., the mean distance traveled by a molecule between collisions with other molecules, is small compared to the characteristic lengths of the fluid system. In the high atmosphere this assumption fails. When an entry vehicle enters a planet's atmosphere it passes through layers with progressive levels of atmospheric gas densification [16]:

- At very high altitudes the atmosphere is rarefied, there are practically no collisions between molecules in the vicinity of the capsule.
- At relative low altitudes the atmosphere is dense with respect to the capsule's size, it behaves as a continuum.

To quantify the rarefaction status of the atmosphere with respect to the capsule's size the Knudsen number is used:

$$Kn_{\infty} = \frac{\lambda_{\infty}}{L_0} \tag{2.1}$$

where λ_{∞} is the mean free path of atmospheric gas molecules and L_0 is a characteristic length of the capsule. The Knudsen number helps determine whether statistical mechanics or continuum mechanics formulation should be used to model a fluid system [16]:

- For $Kn \gg 1$ we have a free molecular flow, and it is described by the statistical theory of gases.
- For $Kn \ll 1$ we have a continuous flow, and it is described by the classical fluid mechanics theory.

Based on the relation existing between Knudsen number, Mach number and Reynolds number we know that the Navier-Stokes system of equations is the proper mathematical model to describe the flow field around an entry capsule during the descent phase:

$$Kn_\infty = \frac{Ma_\infty}{Re_\infty}\sqrt{\frac{\gamma\pi}{2}}, \quad Ma_\infty \ll Re_\infty \quad \Rightarrow \quad Kn_\infty \ll 1 \tag{2.2}$$

2.1 Mathematical model

The mathematical description of the flow field around the ExoMars capsule wich the current numerical model is based on is provided by the Navier-Stokes system of equations derived for an ideal gas. The governing equations of compressible flows can be written in the conservative form:

$$\begin{aligned}
&\frac{\partial \rho}{\partial t} = -\frac{\partial \rho u_j}{\partial x_j} \\
&\frac{\partial \rho u_i}{\partial t} = -\frac{\partial}{\partial x_j}\left(\rho u_i u_j + p\delta_{ij}\right) + \frac{\partial \sigma_{ij}}{\partial x_j} \\
&\frac{\partial \rho E}{\partial t} = -\frac{\partial}{\partial x_j}\left((\rho E + p)u_j\right) + \frac{\partial}{\partial x_j}\left(\lambda\frac{\partial T}{\partial x_j} + \sigma_{ij}u_i\right)
\end{aligned} \tag{2.3}$$

where ρ represents density, u_i represents the $i-th$ velocity component, p represents pressure, T represents temperature, E represents total energy, and lastly σ_{ij} represents the viscous stresses tensor, wich for newtonian – stokesian fluids can be expressed as:

$$\sigma_{ij} = 2\mu e_{ij} - \frac{2}{3}\mu\frac{\partial u_k}{\partial x_k}\delta_{ij}, \qquad e_{ij} = \frac{1}{2}\left(\frac{\partial u_i}{\partial x_j} + \frac{\partial u_j}{\partial x_i}\right) \tag{2.4}$$

where μ and λ represents, respectively, dynamic viscosity and thermic diffusivity. Dynamic viscosity is calculated using a power-law formulation [17]:

$$\mu = K\left(\frac{\partial u}{\partial y}\right)^{n-1} \tag{2.5}$$

$$\lambda = \frac{\mu c_p}{Pr} \tag{2.6}$$

The system consists of five equations with seven unknown variables $(\rho, \rho u_i, \rho E, p, T)$ and needs to be completed using an equation of state for the fluid $\rho = \rho(p, T)$ and a constitutive equation for the internal energy. For an ideal gas we have:

$$\frac{p}{\rho} = RT \tag{2.7}$$

where R is the specific gas constant while the total energy can be written as:

$$E = e + \frac{1}{2}(u_i u_i) \tag{2.8}$$

Total energy is the sum of kinetic energy $\frac{1}{2}(u_i u_i)$ and internal energy e wich, for an ideal gas, is a function of the temperature:

$$e = c_v T = \frac{pR}{\gamma - 1} \tag{2.9}$$

By applying the Buckingham theorem, we can obtain the non-dimensional formulation of the governing equations wich is regulated by four non-dimensional groups. The reference quantities (L_0, ρ_0, T_0, R_0) are set to the unit (notes that the non-dimensional variables are written with the notation $(\cdot)'$):

$$\frac{\partial \rho'}{\partial t'} = -\frac{\partial \rho' u'_j}{\partial x'_j}$$

$$\frac{\partial \rho' u'_i}{\partial t'} = -\frac{\partial}{\partial x'_j}\left(\rho' u'_i u'_j + p' \delta_{ij}\right) + \frac{\sqrt{\gamma} Ma_\infty}{Re_\infty}\frac{\partial \sigma'_{ij}}{\partial x'_j} \tag{2.10}$$

$$\frac{\partial \rho' E'}{\partial t'} = -\frac{\partial}{\partial x_j}\left((\rho' E' + p')u'_j\right) + \frac{\sqrt{\gamma} Ma_\infty}{Re_\infty}\left(\frac{\gamma}{\gamma - 1}\frac{1}{Pr_\infty}\frac{\partial}{\partial x'_j}\left(\lambda' \frac{\partial T'}{\partial x'_j}\right) + \frac{\partial\left(\sigma'_{ij} u'_i\right)}{\partial x'_j}\right)$$

$$\gamma = \frac{c_p}{c_v} \qquad ratio\ between\ specific\ heats\ of\ the\ fluid$$

$$Ma_\infty = \frac{u_\infty}{\sqrt{\gamma R_0 T_0}} \qquad Mach\ number\ of\ the\ undisturbed\ flow \tag{2.11}$$

$$Re_\infty = \frac{\rho_0 u_\infty L_0}{\mu_\infty} \qquad Reynolds\ number\ of\ the\ undisturbed\ flow$$

$$Pr_\infty = \frac{\gamma R_0}{\gamma - 1}\frac{\mu_\infty}{\lambda_\infty} \qquad Prandtl\ number\ of\ the\ undistrubed\ flow$$

2.2 Numerical treatment

The Navier-Stokes system of equations represents an analytical description of flows, but fluid dynamical simulations are carried out on computers, so a numerical treatment is required. This is done by converting differential equations defined in continuous space and time to a system of equations in a discretized domain. The computational domain is discretized in a certain number of nodes by a grid (mesh) while the computational time interval is subdivided in a certain number of time steps. For numerical applications the governing equations are expressed in a vectorial formulation:

$$\frac{\partial \boldsymbol{\Phi}'}{\partial t'} = -\frac{\partial \boldsymbol{C}'_j(\boldsymbol{\Phi}')}{\partial x'_j} + \frac{\partial \boldsymbol{D}'_j(\boldsymbol{\Phi}')}{\partial x'_j} \ , \qquad j = 1,2,3 \tag{2.12}$$

Thus, the system can be seen as a summation of:

- A temporal contribution, related to the temporal variation of the of conservative variables.

$$\boldsymbol{\Phi}' = \begin{pmatrix} \rho' \\ \rho' u'_i \\ \rho' E' \end{pmatrix} \tag{2.13}$$

- A convective contribution, related to the transport phenomena associated to velocity and pressure fields.

$$\boldsymbol{C}'_j(\boldsymbol{\Phi}') = \begin{pmatrix} \rho' u'_i \\ \rho' u'_i u'_j + p' \delta_{ij} \\ (\rho' E' + p') u'_i \end{pmatrix} \tag{2.14}$$

- A diffusive contribution, related to mutual relations between elementary fluid volumes and the thermodynamical behavior of the gas.

$$\boldsymbol{D}'_j(\boldsymbol{\Phi}') = \frac{\sqrt{\gamma} Ma_\infty}{Re_\infty} \begin{pmatrix} 0 \\ \sigma'_{ij} \\ \frac{\gamma}{\gamma - 1} \frac{1}{Pr} \lambda' \frac{\partial T'}{\partial x'_i} + \sigma'_{ij} u'_j \end{pmatrix} \tag{2.15}$$

The solver employed to carry out the simulations of the wake flow is STREAmS, a numerical code developed by Bernardini et al. [18]. STREAmS is validated for three types of canonical compressible flows: supersonic plane channel flow, supersonic boundary layer, shock wave/boundary layer interaction. Results are compared with experimental and numerical data from literature. The solver discretizes the convective terms using a hybrid energy-preserving/shock-capturing scheme in locally conservative form. Take for example the convective flux along the x-direction:

$$f_x = \rho u \varphi \tag{2.16}$$

where φ is the transported quantity ($\varphi = 1$ for the mass equation, $\varphi = u_j$ for the momentum equation in the $j - th$ direction, $\varphi = E + p/\rho$ for the energy equation). The streamwise derivative of f_x on a uniform mesh with spacing Δx is calculated by means of two intermediate nodes:

$$\left. \frac{\partial f_x}{\partial x} \right|_i = \frac{1}{\Delta x} \left(\hat{f}_{x,\ i+1/2} - \hat{f}_{x,\ i-1/2} \right) \tag{2.17}$$

A three-point averaging operator is defined to calculate the energy-preserving numerical flux at the interface $i + 1/2$:

$$\left(\widetilde{F, G, J} \right)_{i,l} = \frac{1}{8} (F_i + F_{i+l})(G_i + G_{i+l})(J_i + J_{i+l}) \tag{2.18}$$

and recasting in conservative form the split formulation of the Eulerian fluxes:

$$\hat{f}_{x,\ i+1/2} = 2\sum_{l=1}^{L} a_l \sum_{m=0}^{l-1} (\widetilde{\rho, u, \varphi})_{i-m,\ l} \tag{2.19}$$

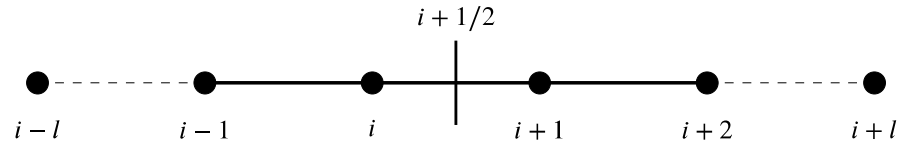

Figure 2.1: sketch of the computational stencil along a generic direction [18].

where a_l are the finite difference coefficients for the first derivative of order $2L$. The locally conservative formulation allows hybridization of the central flux with shock capturing reconstructions. Low-order upwind schemes, wich introduce a lot of numerical dissipation, are shock-capturing but yield to low accuracy in smooth regions (shock-free) of the field. WENO reconstructions allows to capture shocks but maintaining a high-order centered scheme in the rest of the field. The viscous terms are expanded to Laplacian form and approximated with a central finite difference scheme:

$$\frac{\partial}{\partial x}\left(\mu \left.\frac{\partial u}{\partial x}\right|_i\right)\Bigg|_i = \left.\frac{\partial \mu}{\partial x}\right|_i \left.\frac{\partial u}{\partial x}\right|_i + \mu \left.\frac{\partial^2 u}{\partial x^2}\right|_i = \frac{1}{\Delta x^2}\sum_{l=-L}^{L} a_l^2 \mu_{i+l} u_{i+l} + \mu_i \frac{1}{\Delta x^2}\sum_{l=-L}^{L} b_l u_{i+l} \tag{2.20}$$

where b_l are the finite difference coefficients for the second derivative of order $2L$. After the discretization process we have a semi-discrete system of ordinary differential equations (ODE) (one equation for each mesh node ijk):

$$\frac{d\boldsymbol{\Phi}_{ijk}}{dt} = \boldsymbol{R}(\boldsymbol{\Phi}_{ijk}) \tag{2.21}$$

where $\boldsymbol{R}$ is the vector of residuals. The system is advanced in time using a three-stage, third order Runge-Kutta scheme. Thus, the flow field is approximated by a function wich reproduces the time evolution of the flow field variables over the mesh nodes at each time step:

$$\boldsymbol{\Phi}_{ijk}(t_n) \Leftrightarrow \boldsymbol{\Phi}(x, y, z, t) \tag{2.22}$$

where $i = 1, \dots, N_x$, $j = 1, \dots, N_y$ and $k = 1, \dots, N_z$ are the indexes of the mesh nodes positions while $n = 1, \dots, T_n$ is the index of the current time step.

2.3 Comparison between DNS, RANS, and LES

Numerical simulations assume great importance in the field of fluid dynamical analyzes because they allow to predict and to simulate the behavior of systems too complex for an analytical approach, like compressible or incompressible flows. Thanks to Computational Fluid Dynamics (CFD), wich develops numerical methods for the treatment of flows, we can carry out numerical experiments, analogous to actual laboratory experiments, to evaluate the behavior and the properties of the supersonic wake produced by an entry vehicle. The reconstruction of the wake produced by a blunt body is complicated by turbulence, a phenomenon that gives rise to a wide spectrum of vortical structures wich are burdensome to be solved. There are three main approaches depending on the extent to wich turbulence is explicitly described or represented by an a priori model:

- DNS, Direct Numerical Simulations
- RANS, Reynolds – Averaged Navier – Stokes
- LES, Large – Eddy Simulations

The main features of these techniques are exposed and compared below.

2.3.1 Direct Numerical Simulations (DNS)

Direct Numerical Simulations (DNS) directly resolve the Navier – Stokes system of equations without employing any turbulence closure. This kind of approach allows to obtain the most accurate reproduction of turbulent flows because is based on an explicit description of the entire spectrum of vortical structures. The basic requirements for DNS are:

- the mesh spacing and the time step must be fine enough to capture the dynamics of the smallest vortical structures.
- the computational domain and the simulation time must be large enough to capture the dynamics of the largest vortical structures.

The Kolmogorov's K41 theory [14] allows to estimate how the computational cost of a DNS grows with the Reynolds number. For an object with a characteristic dimension L_0, hit by a flow of velocity U_0, the domain must have sizes $L_x \sim L_y \sim L_z \sim L_0$ along x, y and z directions, respectively.

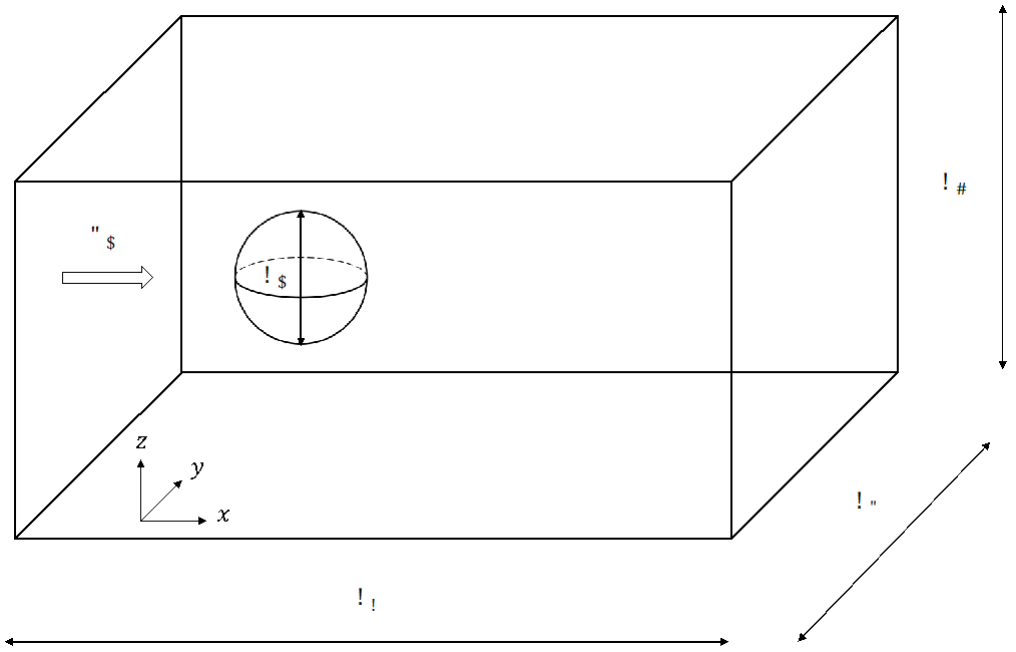

Figure 2.2: sketch of a sphere with a diameter L_0 hit by a flow of velocity U_0 and the relative computational domain.

Taking the x direction, for a uniform, Cartesian grid the spacing must be $\Delta x = L_x/N_x$, where $L_x \sim L_0$ and $\Delta x \sim \eta$ (η represents the Kolmogorov's scale). The total number of grid nodes grows as $Re^{9/4}$:

$$N_x = \frac{L_x}{\Delta x} \sim \frac{L_0}{\eta} \sim Re^{3/4} \tag{2.23}$$

$$N_x \sim N_y \sim N_z \tag{2.24}$$

$$N_{tot} = N_x\, N_y\, N_z \sim Re^{9/4} \tag{2.25}$$

The total number of grid nodes is repeated for $N_{\Delta t}$ times:

$$N_{\Delta t} = \frac{T}{\Delta t} = \frac{T_0}{\tau_\eta} \sim Re^{1/2}\ , \qquad T_0 = \frac{L_0}{U_0} \tag{2.26}$$

where T is the simulation time, Δt is the time step and τ_η is the characteristic time of the Kolmogorov's scale. Finally, we obtain that the computational cost grows about as Re^3:

$$N_{\Delta t}\, N_{tot} \;\propto\; Re^{1/2}\, Re^{9/4} \;=\; Re^{11/4} \sim Re^{3} \tag{2.27}$$

Direct numerical simulations are possible only for flows characterized by moderate Reynolds numbers and are typically exploited on canonical flows studies for basic research on turbulence.

2.3.2 Reynolds-Average Navier-Stokes (RANS)

In contrast to direct numerical simulations, wich fully resolve turbulence, Reynolds-average simulations only resolve the mean flow while all the turbulent scales are treated with an a priori model. The mean flow recovers the symmetries, so a Reynolds-average simulation led to two-dimensional, steady solutions for symmetrical and steady boundary conditions. Indeed, the gradients characterizing the mean flow requires much coarser meshes than a DNS. The computational cost is drastically reduced, making the RANS approach suitable for industrial applications. This numerical technique is based on the Reynolds decomposition of the flow field variables. Taking for example the $i-th$ velocity component $u_i(\bar{x},t)$, it can be expressed as the sum of the mean velocity $U_i(\bar{x},t)$ and the residual fluctuating velocity $u_i{}'(\bar{x},t)$:

$$u_i(\bar{x},t) = U_i(\bar{x},t) + u_i{}'(\bar{x},t)\ , \qquad U_i(\bar{x},t) = \langle u_i(\bar{x},t)\rangle \tag{2.28}$$

The mean operator is a Reynolds operator and has a set of properties:

$$\langle u_i{}'(\bar{x},t)\rangle = 0 \tag{2.29}$$

$$\langle U_i(\bar{x},t)\rangle = U_i(\bar{x},t) \tag{2.30}$$

A Reynolds-average simulation solve the Reynolds-Average Navier-Stokes (RANS) equations wich are derived by applying the Reynolds operator to the governing equations. The key issue of this approach arises from the impossibility to close the system of RANS equations. Let's consider the incompressible case:

$$\frac{\partial u_i}{\partial x_i} = 0$$
$$\frac{\partial u_i}{\partial t} + \frac{\partial}{\partial x_j}(u_i u_j) = -\frac{1}{\rho}\frac{\partial p}{\partial x_i} + \frac{\partial}{\partial x_j}(2\nu e_{ij}) \tag{2.31}$$

RANS equations govern the mean flow and are derived by applying the Reynolds operator at both the left-hand-side and right-hand-side of the Navier-Stokes system of equations:

$$\frac{\partial U_i}{\partial x_i} = 0 \qquad \left(\frac{\partial u_i{}'}{\partial x_i} = 0\right)$$
$$\frac{\partial U_i}{\partial t} + \frac{\partial}{\partial x_j}(U_i U_j) = -\frac{1}{\rho}\frac{\partial P}{\partial x_i} + \frac{\partial}{\partial x_j}(2\nu E_{ij}) - \frac{\partial}{\partial x_j}\langle u_i{}' u_j{}'\rangle \tag{2.32}$$

Now we have four equations and ten unknown variables: P, U_i and the six independent components of the Reynolds stresses tensor (the tensor is symmetrical):

$$\langle u_i{}' u_j{}'\rangle = \begin{bmatrix} \langle u'^2\rangle & \langle u'v'\rangle & \langle u'w'\rangle \\ \langle v'u'\rangle & \langle v'^2\rangle & \langle v'w'\rangle \\ \langle w'u'\rangle & \langle w'v'\rangle & \langle w'^2\rangle \end{bmatrix} \tag{2.33}$$

The Reynolds stresses tensor follow from the application of the Reynolds operator to the convective term:

$$\langle \frac{\partial}{\partial x_j}(u_i u_j)\rangle = \langle \frac{\partial}{\partial x_j}\left[(U_i + u_i{}')(U_j + u_j{}')\right]\rangle =$$

$$= \frac{\partial}{\partial x_j}\left[\langle U_i U_j\rangle + \langle U_i u_j{}'\rangle + \langle u_i{}' U_j\rangle + \langle u_i{}' u_j{}'\rangle\right] =$$

$$= \frac{\partial}{\partial x_j}(U_i U_j) + \frac{\partial}{\partial x_j}\langle u_i{}' u_j{}'\rangle \tag{2.34}$$

It's not possible to close the system form first principles, thus it's necessary to find a model for the Reynolds stresses in terms of mean flow quantities. This can be reached by decomposing the Reynolds stresses tensor in its spheric and its deviatoric part:

$$-\langle u_i' u_j' \rangle = -\frac{2}{3} k \delta_{ij} + b_{ij} \, , \quad k = \frac{1}{2} \langle u_i' u_i' \rangle \tag{2.35}$$

where k is the turbulent kinetic energy and b_{ij} is the deviatoric part. In 1887, Boussinesq [19] formulated the turbulent – viscosity hypothesis that says: the principal effect of the Reynolds stresses is to add a "turbulent" viscosity to the flow. By analogy with molecular viscosity:

$$\tau_{ij} = -p\delta_{ij} + 2\nu e_{ij} \, , \qquad e_{ij} = \frac{1}{2}\left(\frac{\partial u_i}{\partial x_j} + \frac{\partial u_j}{\partial x_i}\right) \tag{2.36}$$

where ν is the cinematic (molecular) viscosity, and it's a fluid property, the deviatoric part of the Reynolds stresses tensor become proportional to the mean deformation tensor:

$$-\langle u_i' u_j' \rangle = -\frac{2}{3} k \delta_{ij} + 2\nu_T E_{ij} \, , \qquad E_{ij} = \frac{1}{2}\left(\frac{\partial U_i}{\partial x_j} + \frac{\partial U_j}{\partial x_i}\right) \tag{2.37}$$

where ν_T is the turbulent viscosity and it depends on the flow field. Now we have four equations and five unknown variables (P, U_i and $\nu_T(\bar{x}, t)$). It's necessary to introduce a model for the turbulent viscosity yielding to a certain number of arbitrary constants. The nature of the assumptions underlying a Reynolds – average closure causes that the results of such simulations are not always regarded with data, and experimental support is required for confidence.

2.3.3 Large-Eddy Simulations (LES)

Large-eddy simulations are on some middle ground between direct numerical and Reynolds-average simulations because they only resolve large vortical structures. This kind of approach finds its reason to be in the fact that the statistics of the largest scales ($l \sim L_0$) are dependent on the geometry of the fluid system while the statistics of the small scales ($l \ll L_0$) are universal. Thus, large-eddy simulations allow simultaneously to treat high Reynolds number flows and to obtain a precise reproduction of turbulence. Conceptually, a low-pass filter is applied to the flow field variables, then only turbulent motions larger than the filter scale are explicitly described. The large-eddy approach goes through three main steps:

1. Define a filtering operator G_Δ to decompose flow field variables into the sum of a filtered term, representing the motion of large eddies, and a residual term, representing the motion of small eddies.
2. Apply the filtering operator to the Navier-Stokes equations to derive the governing equations of the filtered flow field.
3. Solve the filtered Navier-Stokes equations to obtain a simulation of large eddies characterizing the turbulent flow.

Being $\bar{\phi}$ a filtered fluid dynamic variable, the Favre filter of ϕ is defined as:

$$\tilde{\phi} = \frac{\overline{\rho\phi}}{\bar{\rho}} \tag{2.38}$$

Based on the definition of the Favre filter, the filtered non-dimensional Navier-Stokes system of equations for compressible flows is derived as follows [20]:

$$\begin{aligned}
&\frac{\partial \bar{\rho}}{\partial t} = -\frac{\partial \bar{\rho}\tilde{\mathrm{u}}_\mathrm{j}}{\partial \mathrm{x}_\mathrm{j}} \\
&\frac{\partial \bar{\rho}\tilde{\mathrm{u}}_\mathrm{i}}{\partial \mathrm{t}} = -\frac{\partial}{\partial \mathrm{x}_\mathrm{j}}\left(\bar{\rho}\tilde{\mathrm{u}}_\mathrm{i}\tilde{\mathrm{u}}_\mathrm{j} + \bar{p}_i\delta_{\mathrm{ij}}\right) + \frac{\sqrt{\gamma}Ma_\infty}{Re_\infty}\frac{\partial}{\partial \mathrm{x}_\mathrm{j}}\left(\bar{\mu}\bar{\sigma}_{ij}\right) - \frac{\partial}{\partial \mathrm{x}_\mathrm{j}}\left(\overline{\rho u_\imath u_J} - \bar{\rho}\tilde{u}_i\tilde{u}_j\right) \\
&\frac{\partial \bar{\rho}\widetilde{\mathrm{E}}}{\partial \mathrm{t}} = -\frac{\partial}{\partial \mathrm{x}_\mathrm{j}}\left(\left(\bar{\rho}\widetilde{\mathrm{E}} + \tilde{\mathrm{p}}\right)\tilde{u}_\mathrm{j}\right) + \frac{\sqrt{\gamma}Ma_\infty}{Re_\infty}\left(\frac{\gamma}{\gamma-1}\frac{1}{Pr_\infty}\frac{\partial}{\partial \mathrm{x}_\mathrm{j}}\left(\mathrm{k}\frac{\partial \widetilde{\mathrm{T}}}{\partial \mathrm{x}_\mathrm{j}}\right) + \frac{\partial}{\partial \mathrm{x}_\mathrm{j}}\left(\bar{\mu}\bar{\sigma}_{ij}\tilde{u}_i\right)\right) \\
&\qquad -\frac{\partial}{\partial x_j}\left(\overline{(\rho E + p)u_\imath} - \left(\bar{\rho}\tilde{E} + \bar{p}\right)\tilde{u}_i\right)
\end{aligned} \tag{2.39}$$

Comparing the current system to the original non-filtered formulation it can be found an additional term in the momentum conservation equation and an additional term in the energy conservation equation. These terms are, respectively, the divergence of the subgrid-scale (SGS) stress tensor, expressed as:

$$\bar{T}_{ij}^{SGS} = \overline{\rho u_\imath u_J} - \bar{\rho}\tilde{u}_i\tilde{u}_j \tag{2.40}$$

and the divergence of the subgrid-scale (SGS) energy term, expressed as:

$$\bar{E}_j^{SGS} = \overline{(\rho E + p)u_\iota} - \left(\bar{\rho}\tilde{E} + \tilde{p}\right)\tilde{u}_i = \overline{\rho c_p T u_J} - \bar{\rho}\bar{c_p}\tilde{T}\tilde{u}_j + \frac{1}{2}\bar{T}_{ij}^{SGS}\tilde{u}_j - \frac{1}{2}\bar{T}_{kk}^{SGS}\tilde{u}_j \qquad (2.41)$$

wich represent the under resolved, residual terms of the filtering process. The treatment of the subgrid terms lead to two different LES techniques:

- Explicit LES: residual terms are treated with an a priori model. Explicit descriptions of subgrid-scale terms were proposed by Smagorinski [21] or Nicoud and Ducros [22] who brought the Wall-Adaptive Large-Eddy viscosity model (WALE).
- Implicit LES: the effect of residual terms is emulated by the intrinsic numerical dissipation. The implicit LES approach is followed in this work to simulate the wake region. An example of implicit LES implementation can be found in the work carried out by Bernardini et al. [24].

2.4 Immersed Boundary Method

The term "Immersed Boundary Method" (IBM) refers to a numerical approach originally developed by Peskin [25] in his studies regarding cardiac mechanics and the relative blood flow. Peskin's idea was to remove the process of re-meshing at each time step by performing simulations on a fixed, Cartesian grid wich did not conform to the geometry of the heart. Then, a novel procedure was formulated to impose the effect of the immersed boundary on the flow. The conventional approach makes use of structured or unstructured grids fitting the solid boundaries. First, a surface grid covering the boundaries is generated, then the surface nodes are employed as reference points to generate a volume grid that covers the fluid domain by excluding the body. In contrast, the current approach makes use of Cartesian grids covering the entire fluid domain and including the volume occupied by the body. A structured, non-body conformal grid is obtained, and the immersed boundary is represented by a surface grid by means of that fluid nodes and solid nodes are identified. In this case wall conditions must be imposed indirectly through a modification of the Navier – Stokes equations because the mesh did not adhere to the body's surface. An immersed boundary method allows to ease the meshing process and to increase the computational efficiency using structured, Cartesian grids. The problem consists in the fact that imposing the boundary conditions is not straightforward in IB methods. In addition, alignment between the grid lines and the body surface in body – conformal grids allow better control of the grid resolution in the vicinity of the body [26].

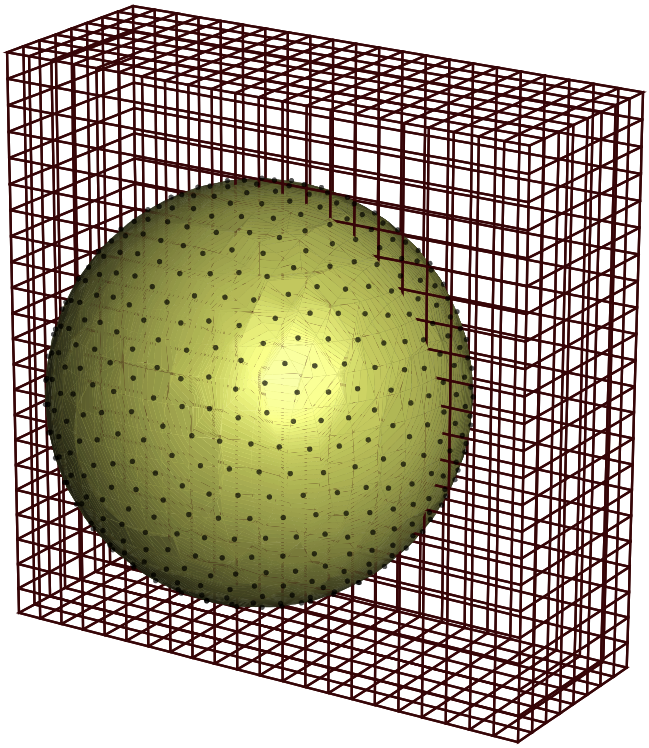

Figure 2.3: Eulerian grid and distribution of the Lagrangian grid points over a sphere for an IBM module [28].

Although the use of body – fitted unstructured grids provides a highly effective meshing strategy, for this work an immersed boundary method is considered because [29]:

- Robust and reliable high – resolution schemes are easily implemented on structured Cartesian grids.
- There is some numerical evidence that for strong shocks, standard numerical schemes applied on unstructured grids suffer from dispersive and dissipative errors larger than those resulting from the use of high – resolution schemes on structured grids.

Since Peskin introduced this method, numerous modifications and refinements have been proposed [27, 28, 29]. In most of them, the concept is to use a Eulerian mesh for the flow field simulation, wich is coupled with a Lagrangian representation of the immersed boundary. The Lagrangian points can move, or not (fixed geometries), independently of the Eulerian flow, and the corresponding immersed boundary exerts a singular force on the fluid. IB methods are proven to ease the meshing process, especially for flows investing moving objects. Uhlmann [27] developed an IBM that proved computational efficiency for simulations of particle laden viscous incompressible flows. It works by means of two distinct grids: a fixed, uniform, Cartesian grid, referred as the Eulerian grid, coupled to a

moving, surface grid, referred as the Lagrangian grid, attached to the particles. Boundary conditions on the surface of a particle cannot be imposed directly but instead by forcing the governing equations with a term wich activates in the vicinity of the particle.

2.4.1 The Direct Forcing Method

The Direct Forcing Method (DFM), firstly introduced by Uhlmann [27], consists of directly forcing the Navier – Stokes system of equations by adding a source term that simulates the presence of a solid body. Let's consider the vectorial formulation of the system:

$$\frac{\partial \boldsymbol{\Phi}}{\partial t} + \frac{\partial \boldsymbol{C}_j(\boldsymbol{\Phi})}{\partial x_j} - \frac{\partial \boldsymbol{D}_j(\boldsymbol{\Phi})}{\partial x_j} = \boldsymbol{S}(\boldsymbol{\Phi}) \tag{2.42}$$

Being $\{\boldsymbol{x}_b^l\}_{l=1}^n$ a collection of Lagrangian points, such as the surface nodes covering the immersed boundary, the source term can be expressed as:

$$\boldsymbol{S}(\boldsymbol{\Phi}) = \{0, \rho\mathcal{F}_i, \rho\mathcal{F}_i u_i\}^T, \qquad i = 1, \dots, 3 \tag{2.43}$$

where $\mathcal{F}_i$ is an Eulerian field defined as:

$$\mathcal{F}_i(\boldsymbol{x}) = \begin{cases} u_i - \bar{u}_i^l & if \quad \|\boldsymbol{x} - \boldsymbol{x}_b^l\| \to 0 \\ 0 & if \quad \|\boldsymbol{x} - \boldsymbol{x}_b^l\| \to \infty \end{cases} \tag{2.44}$$

Here u_i and $\bar{u}_i^l$ represent, respectively, the velocity component along the $i-th$ direction and a target velocity at the boundary location $\boldsymbol{x}_b^l$. In this way, the source term act as a dumping contribution, forcing the solution of the Navier – Stokes system of equations to respect the wall conditions. From a numerical point of view, forced equations are commonly treated with a predictor – corrector strategy:

- First, a predictor step integrates the equations without considering the source term, computing a guess solution $\boldsymbol{\Phi}^*$ that solve the system:

$$\frac{\partial \boldsymbol{\Phi}^*}{\partial t} + \frac{\partial \boldsymbol{C}_j(\boldsymbol{\Phi}^*)}{\partial x_j} - \frac{\partial \boldsymbol{D}_j(\boldsymbol{\Phi}^*)}{\partial x_j} = 0 \tag{2.45}$$

- Then, a corrector step imposes the source term by solving the equation:

$$\frac{\partial \boldsymbol{\Phi}^*}{\partial t} = \boldsymbol{S}(\boldsymbol{\Phi}^*) \tag{2.46}$$

2.4.2 The Ghost Point Forcing Method

The Ghost Point Forcing Method (GPFM) consists of directly modifying the flowfield variables in the vicinity of the body-fluid interface to impose the wall conditions. That is implemented by means of a set of points, called ghost points, hidden behind the immersed boundary. The DFM represent an optimal strategy to impose Dirichlet boundary conditions and solve pressure and velocity fields. The GPFM instead can deal with both Dirichlet and Neumann boundary conditions and is efficient for imposing no-flux boundary conditions like adiabatic boundary conditions or impermeable conditions. The computational scheme that we can find in the work presented by Boukharfane et al. [29] goes through the following main steps:

- Identification of the ghost points within the solid boundaries.
- From each ghost point, a vector normal to the nearest boundary segment is built to locate the image of the corresponding ghost point in the fluid domain.
- The values of the flow field variables at each image point are interpolated from the surrounding grid points.
- The interpolated values obtained for the image points are used to settle the values at the corresponding ghost points to ensure the desired boundary conditions at the fluid – solid interface.

Firstly, the immersed boundary must be represented by a set of Lagrangian points. The solid's surface is discretized as a polyhedron employing the stereo – lithography format (STL). As shown in figure 2., the coordinates of the three vertices S_k of each elementary triangle T_l allow to define the associated Lagrangian point as its center of gravity. Once the Cartesian computational grid is generated, a flagging step that discriminates between fluid and solid nodes is performed: given a point P with coordinates (x_1, x_2, x_3) and a polyhedron, P is a solid node if it is located inside the polyhedron and viceversa. The point – in – polyhedron identification can be carried out by tracing a line from P to any point S, wich is located sufficiently far from the polyhedron, and then counting the total number of intersections. If

the number of intersections is odd then the point is located inside the polygon, it is located outside otherwise.

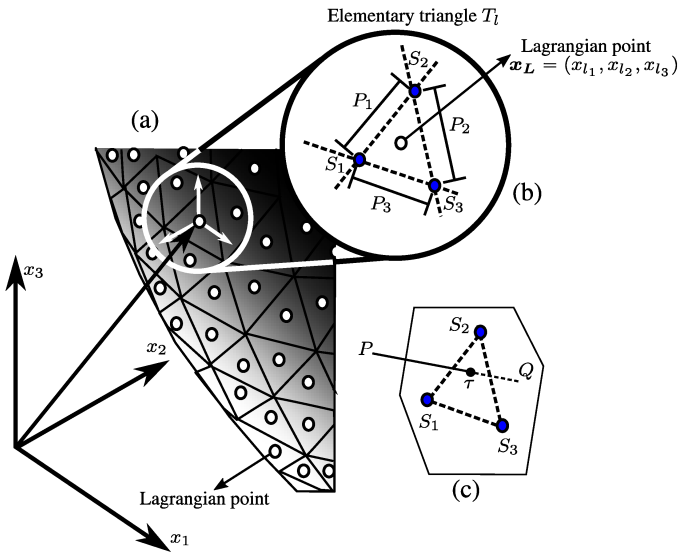

Figure 2.4: sketch of discretized representation of the solid boundary [29].

Thus, an integer marker field is initialized to identify the fluid Ω_F and solid Ω_S domains:

$$\xi(x,t) = \begin{cases} 0 \;\; if \;\; \boldsymbol{x} = (x_1, x_2, x_3)^t \;\in\; \Omega_F \\ 1 \;\; if \;\; \boldsymbol{x} = (x_1, x_2, x_3)^t \;\in\; \Omega_{GP} \\ 2 \;\; if \;\; \boldsymbol{x} = (x_1, x_2, x_3)^t \;\in\; \Omega_S \end{cases} \tag{2.47}$$

where the subset Ω_{GP} correspond to the ghost points that are defined in the solid domain. More specifically, ghost points are defined as solid points having neighboring fluid points:

$$\Omega_{GP} = \left\{ \left(x_{1,m}, x_{2,n}, x_{3,p}\right)^t \in \Omega_S \;\; if \; \exists \left(x_{1,i}, x_{2,j}, x_{3,k}\right)^t \in \Omega_F \;\; such\ that\ i \in I_m \vee \; j \in I_n \vee \; k \in I_p \right\}$$

We can define multiple layers of ghost points behind the immersed boundary to build proper computational stencils for high order finite difference schemes:

$$\begin{aligned} I_m &= [m - l, m + l] \\ I_n &= [n - l, n + l] \\ I_p &= [p - l, p + l] \end{aligned} \tag{2.48}$$

The values of the flow field variables at the embedded ghost points are imposed by using the values at the neighboring fluid nodes. As shown in figure 2., from each ghost point a vector normal to the nearest boundary triangle is built to locate the image of the corresponding ghost point that belongs to the fluid domain. The flow field variables at each image point are then interpolated from the surroundings computational nodes. The corresponding flow field variables are subsequently used to set variables at ghost points to ensure the requisite boundary conditions. From a general point of view, the specification of the boundary conditions may be considered based on the following transport equation:

$$a\frac{\partial \varphi}{\partial n} + b\varphi = c \tag{2.49}$$

where n represents the coordinate along the direction normal to the immersed boundary and c represents the desired boundary value. The value of any conservative variable φ at a ghost point is set from the one calculated at the corresponding image point given the boundary conditions that is desired at the immersed boundary. To impose a Dirichlet type boundary condition the coefficients are set to $a = 0$ and $b = 1$, while for a Neumann type boundary condition they are set to $a = 1$ and $b = 0$.

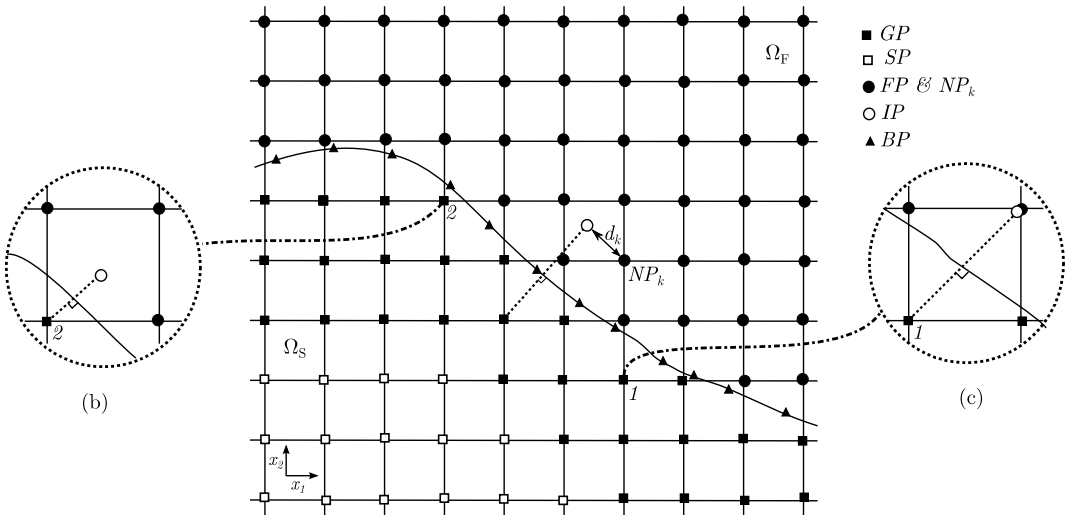

Figure 2.5: Ghost-Point Forcing Method implementation [29].

CHAPTER 3

RESULTS

This chapter presents the results of the simulations computed with STREAmS at various angles of attack: 0°, 5°, 10° and 15°. In accordance with the non-dimensional formulation wich is implemented, the resulting values are non-dimensional and indicate variations of the flow field variables with respect to the upstream flow values. Simulations are set to $Ma_\infty = 2$ and $Re_\infty = 10^6$ to reproduce the flight conditions occurring for the terminal part of the descent phase. Setting parameters were deduced by ExoMars AMELIA investigation of Mars' atmosphere [31]. The computational domain, shown in figure 3.1, is configured as a square cuboid. Domain sizes are $20\,d \times 10\,d \times 10\,d$, where d corresponds to the capsule's maximum diameter. The mesh consists of a Cartesian, non-body conformal, structured grid featuring $2048 \times 672 \times 672$ grid point for a total of 924 844 032 grid points. The distribution of the grid points isn't uniform because are thickened around the capsule to capture the intense gradients characterizing the turbulent wake region.

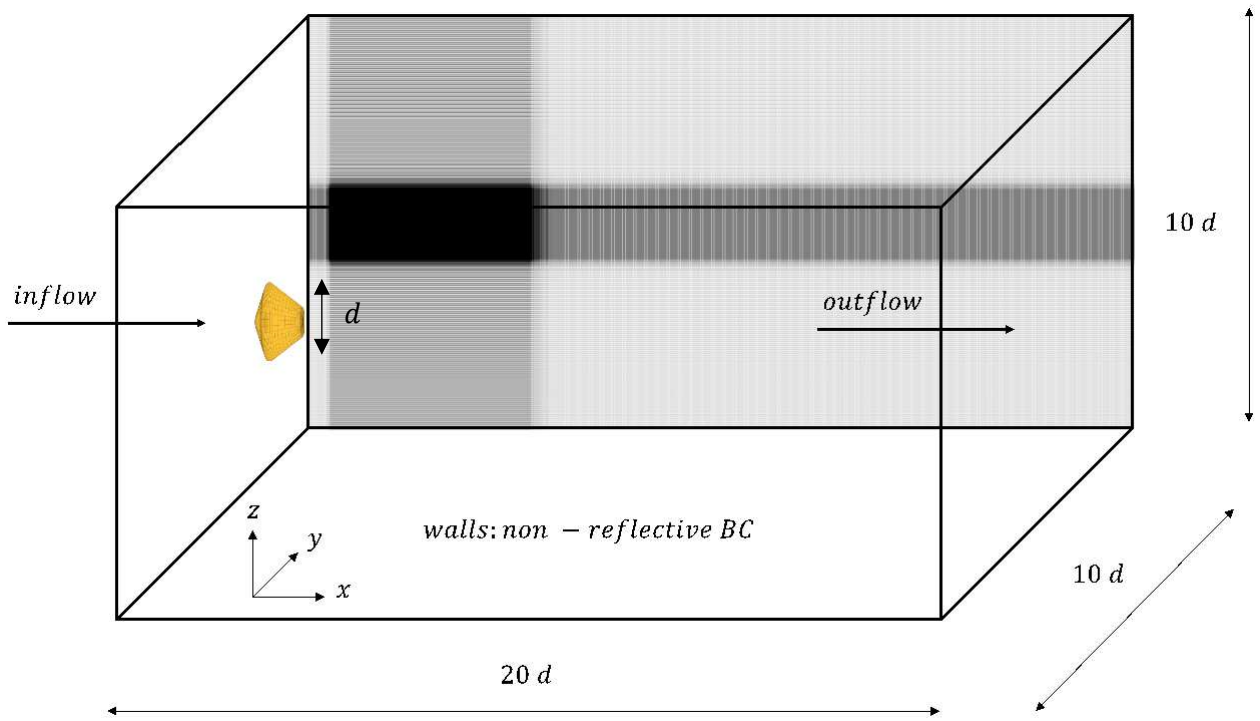

Figure 3.1: sketch of the domain sizes and nodes distribution; on the walls non – reflective boundary conditions are imposed because the capsule flow is not bounded.

1.1 Flow field

The flow field around the capsule is visualized through two-dimensional contours of temperature and density fields snapped at a generic instant in time. Figure 3.2 shows the main features of the supersonic capsule flow:

- The bow shock ahead of the capsule.
- The near – wake recirculation region.
- The recompression shock.
- The vortical structures characterizing the wake.

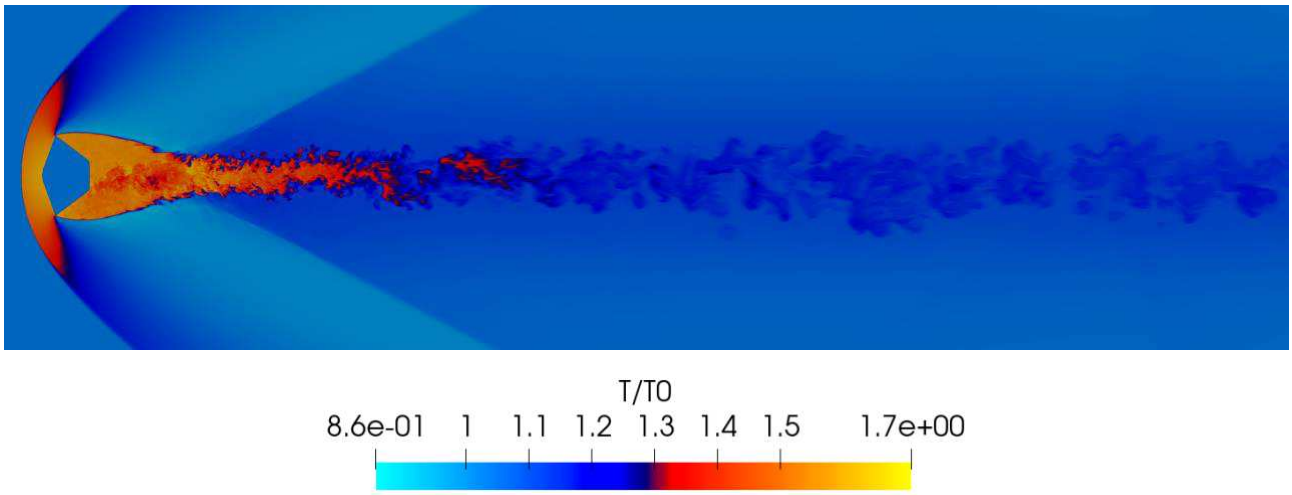

Figure 3.2: temperature field for $AoA = 0°$ (zoom on near capsule flow field features): $Ma_\infty = 2$, $Re_\infty = 10^6$. The bow shock downstream temperature is about 1.5 times higher than upstream temperature, in line with normal shock jump relations at Mach 2.

Temperature (figures 3.3 and 3.4) and density (figures 3.5 and 3.6) instant fields for different angles of attack point out that:

- The wake is deflected from both the axis of the capsule and the direction of the upstream flow by the recompression shock (i.e., for a counterclockwise rotation of the capsule the wake exhibits a clockwise deviation).
- The near wake recirculation region become shorter, and the recompression shock approaches the capsule.

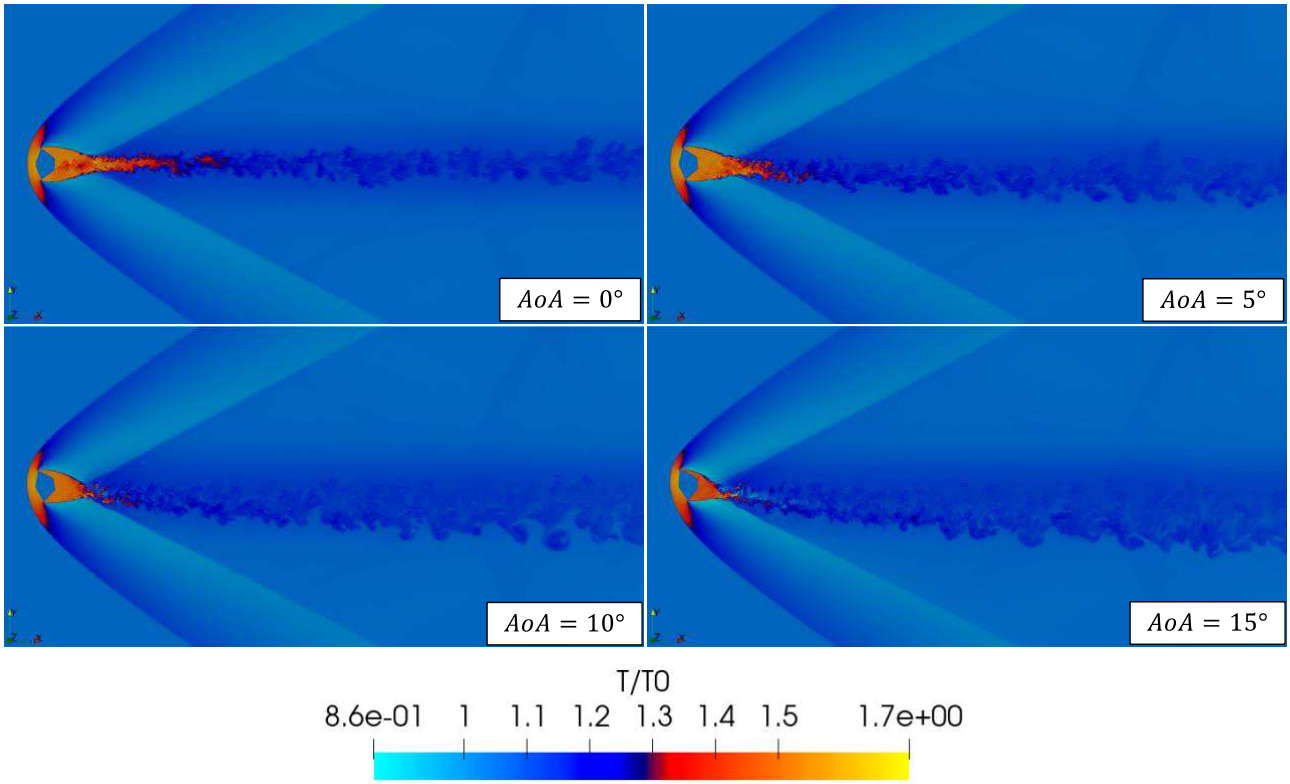

Figure 3.3: temperature field for different angles of attack: $Ma_\infty = 2, Re_\infty = 10^6$.

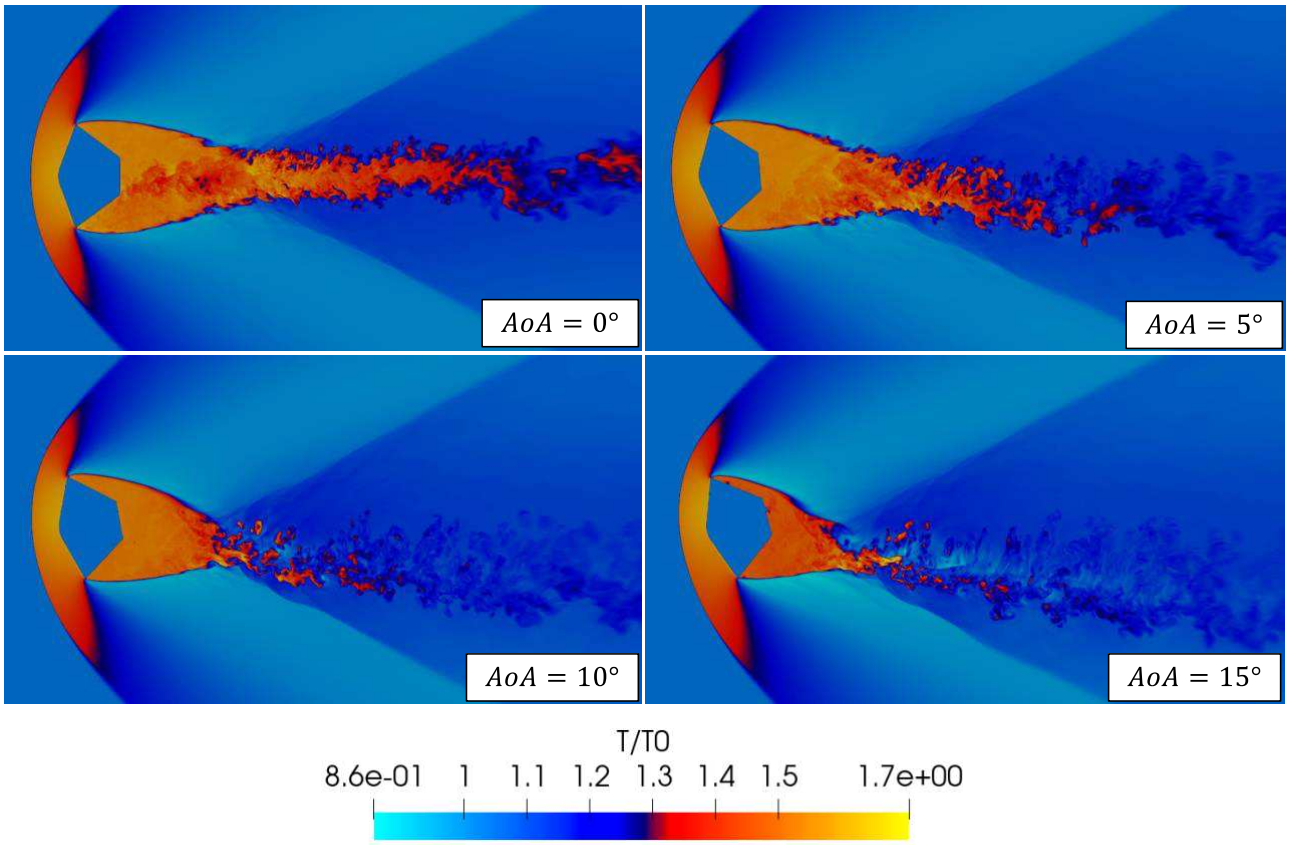

Figure 3.4: temperature field for different angles of attack (zoom on near capsule flow field features): $Ma_\infty = 2, Re_\infty = 10^6$.

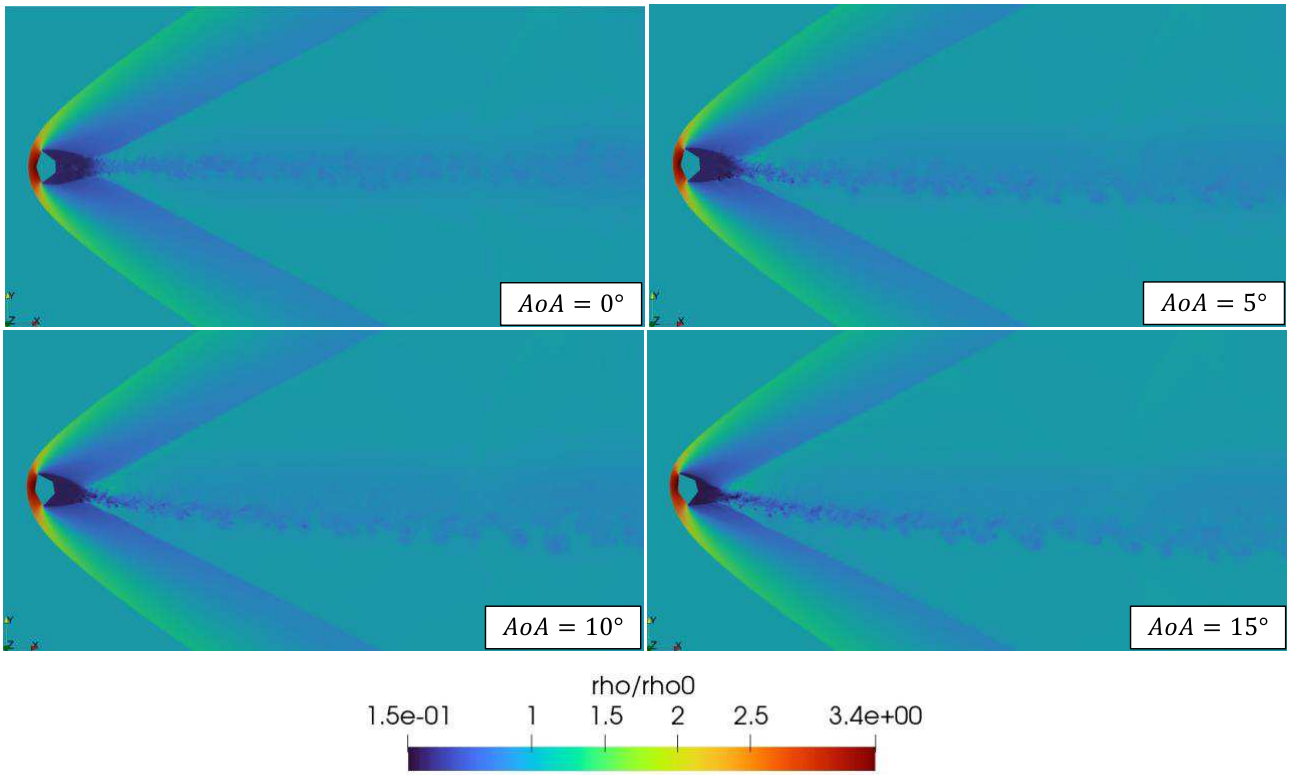

Figure 3.5: density field for different angles of attack: $Ma_\infty = 2, Re_\infty = 10^6$.

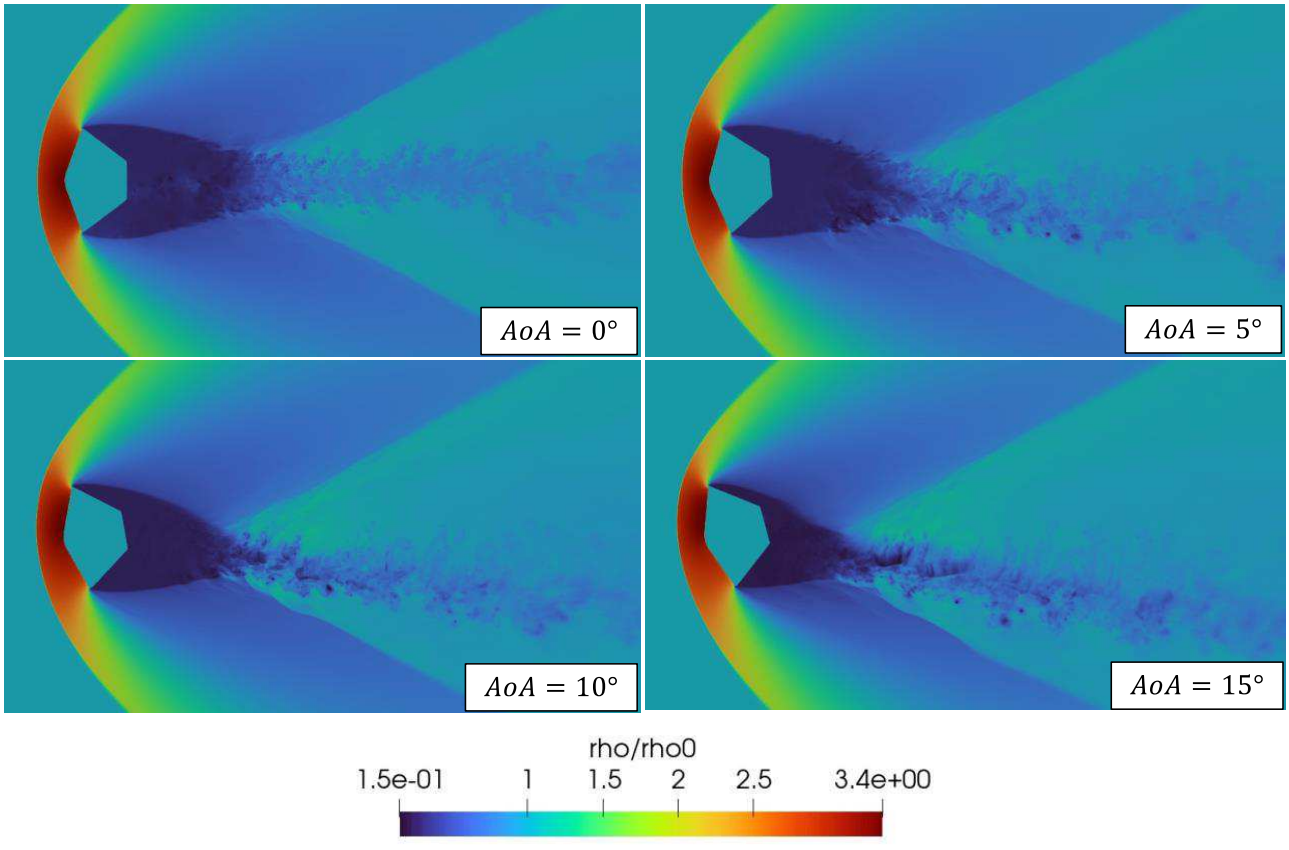

Figure 3.6: density field for different angles of attack (zoom on near capsule flow field features): $Ma_\infty = 2, Re_\infty = 10^6$.

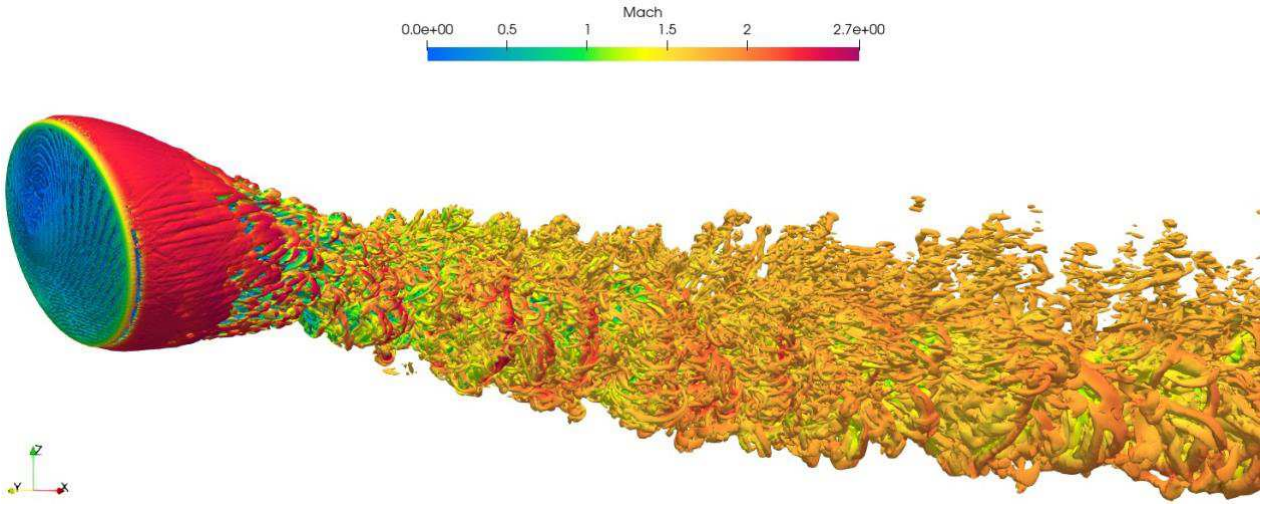

Figure 3.7: visualization of the wake region for $AoA = 5°$ with Q-criterion: $Ma_\infty = 2$, $Re_\infty = 10^6$.

Mean Mach contours reported for different angles of attack, shown in figure 3.8, highlight the supersonic and subsonic regions of the flow field. Contours point out that the subsonic region matches the hot region of the wake (figures 3.3 and 3.4). It can be observed that for a raising angle of attack the extension of the subsonic region become shorter and the recompression shock approaches the capsule. This could be since for a wider angle of attack the capsule cross section becomes tighter, resulting in a closer reattachment of the detached flow.

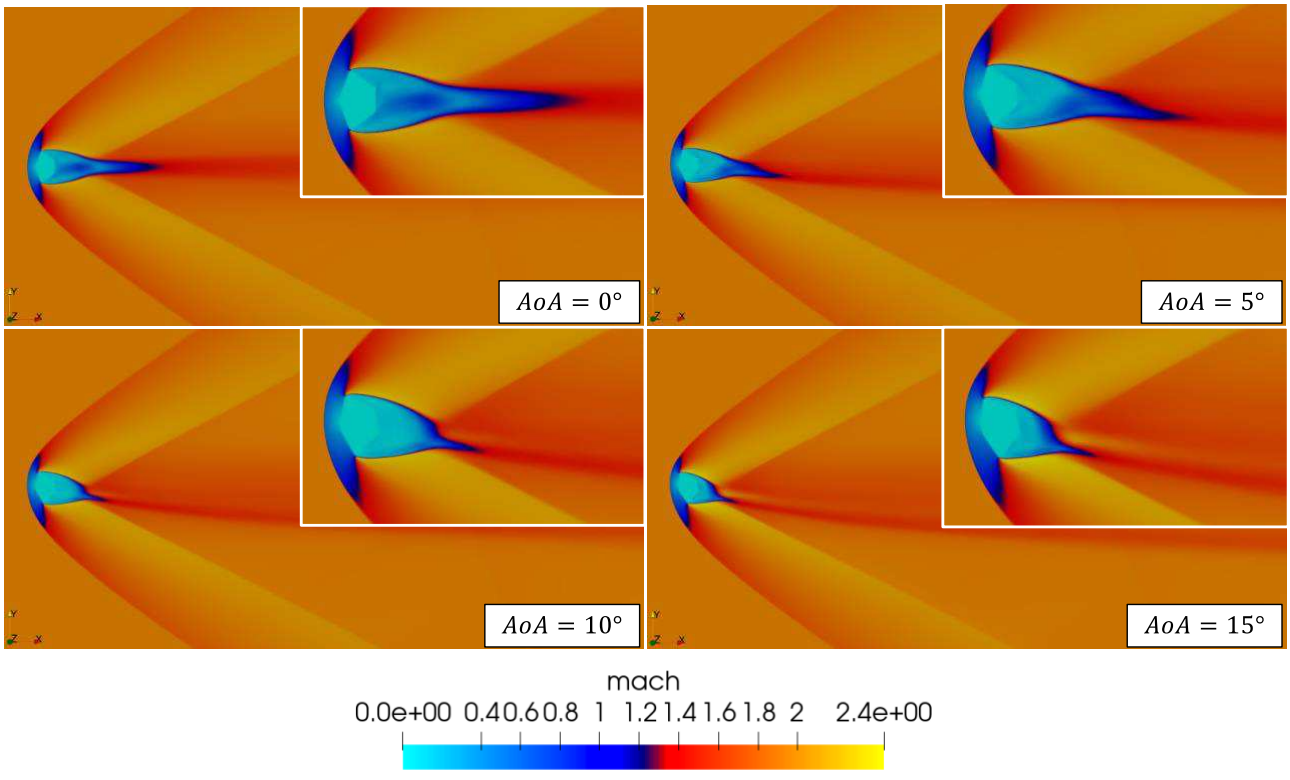

Figure 3.8: Mean Mach contours for different angles of attack (zoom on near capsule flow field features): $Ma_\infty = 2$, $Re_\infty = 10^6$.

Turbulent kinetic energy (eq. 2.35) contours reported for different angles of attack, shown in figure 3.9, highlight the intensity of turbulent fluctuations within the flow field. Both the bow shock and the recompressions shock exhibit a steady behavior. Turbulent fluctuations concentrate in the region where the interaction between recompression shock and wake occurs to then propagate in the wake region. Such interaction is symmetrical for $AoA = 0°$ but become asymmetrical and more intense when the angle of attack increase. Lastly, it can be observed that the wake deflects where turbulent fluctuations are more intense.

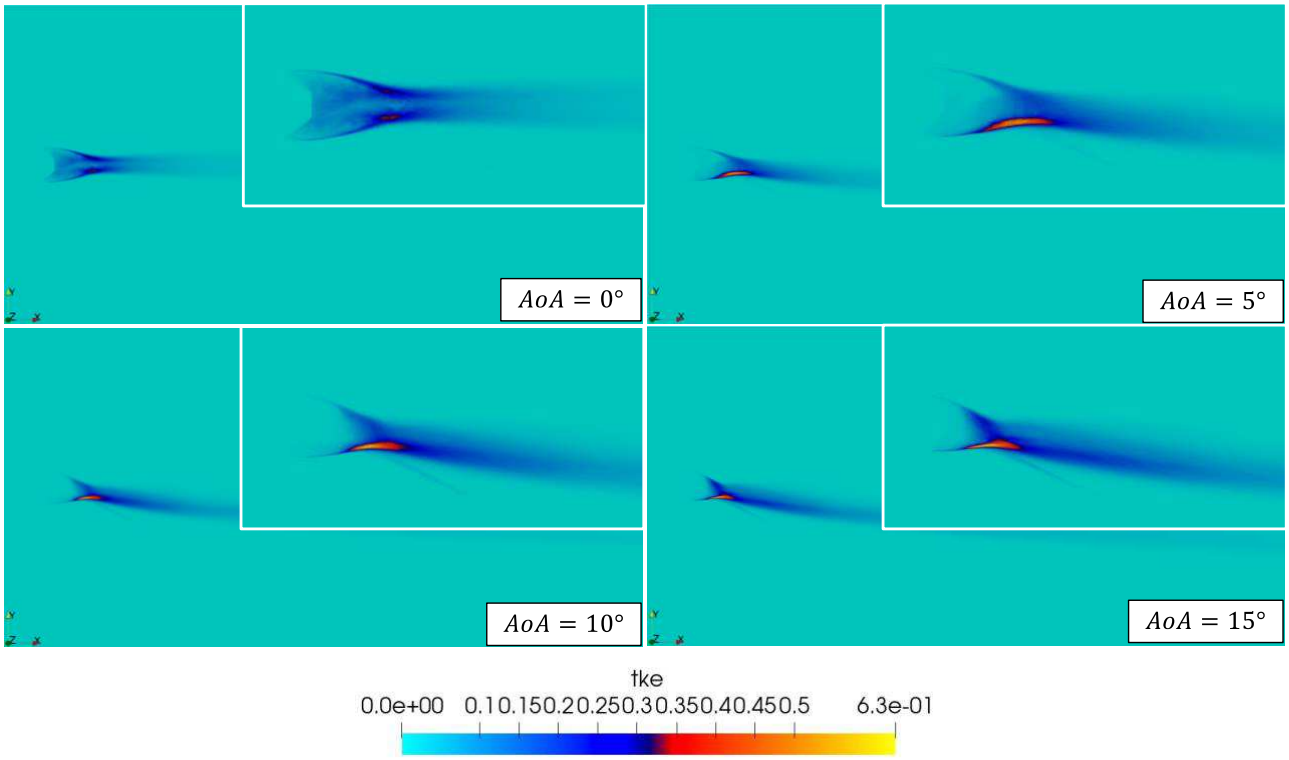

Figure 3.9: turbulent kinetic energy contours for different angles of attack (zoom on near capsule flow field features): $Ma_\infty = 2, Re_\infty = 10^6$.

In figures 3.10 and 3.11 are shown the root mean squares of density and pressure fluctuating fields, respectively. It can be observed strong fluctuations where the interaction between recompression shock and wake occurs. Fluctuations concentrate where the wake is deflected by the recompression shock and intensifies for a raising angle of attack. Indeed, density and pressure fields exhibit fluctuation astride the recompression shock. A further observation consists in the fact that the near wake recirculation region seems to conserve a laminar structure.

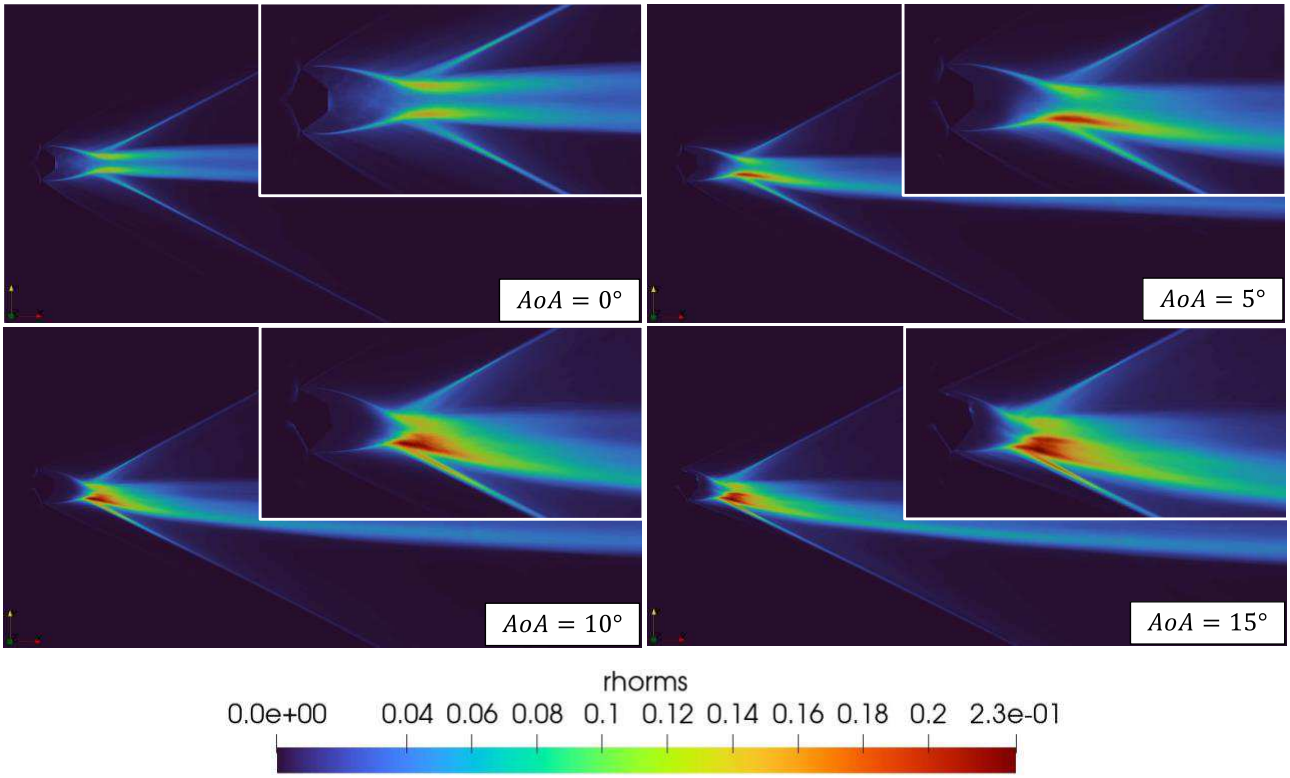

Figure 3.10: root mean square of fluctuating density field for different angles of attack (zoom on near capsule flow field features): $Ma_\infty = 2$, $Re_\infty = 10^6$.

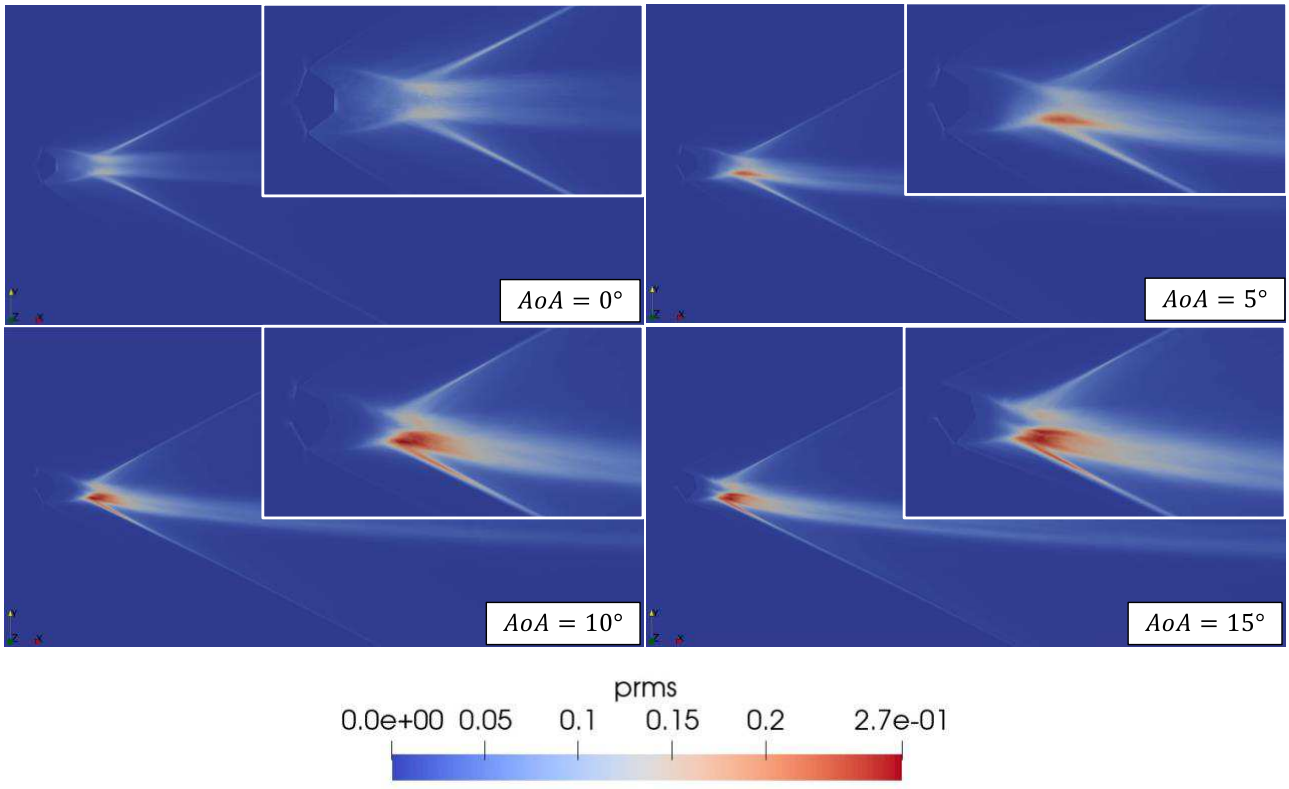

Figure 3.11: root mean square of fluctuating pressure field for different angles of attack (zoom on near capsule flow field features): $Ma_\infty = 2$, $Re_\infty = 10^6$.

1.2 Aerodynamic coefficients

Oscillations in the flow field and their influence on capsule stability are evaluated through temporal evolutions of force and moment coefficients. The temporal evolution of drag coefficient, shown in figure 3.12, is almost constant (oscillations are limited to ~0.5%). The temporal mean value of drag coefficient doesn't change for the different angles of attack that have been simulated: $\overline{C_d} \cong 1.57$. The temporal evolutions of lift and moment coefficients, shown in figure 3.13 and 3.14, exhibit wider fluctuations with respect to drag coefficient. The temporal mean value of lift and moment coefficients raise with the angle of attack (for angles of attack different from $0°$ the flow field become asymmetrical). The Fourier analysis of the temporal evolutions of lift coefficient, shown in figure 3.15, highlight a principal oscillation around a Strouhal number $St = 0.2$ (corresponding to ~25 Hz) wich is repeated for all the angles of attack that have been simulated. High frequency and low frequency patterns are recognizable. It can be observed that for $AoA = 10°$ and $AoA = 15°$ we have a second peak wich moves towards higher frequencies. More in general, for a raising angle of attack the content of higher frequencies increase.

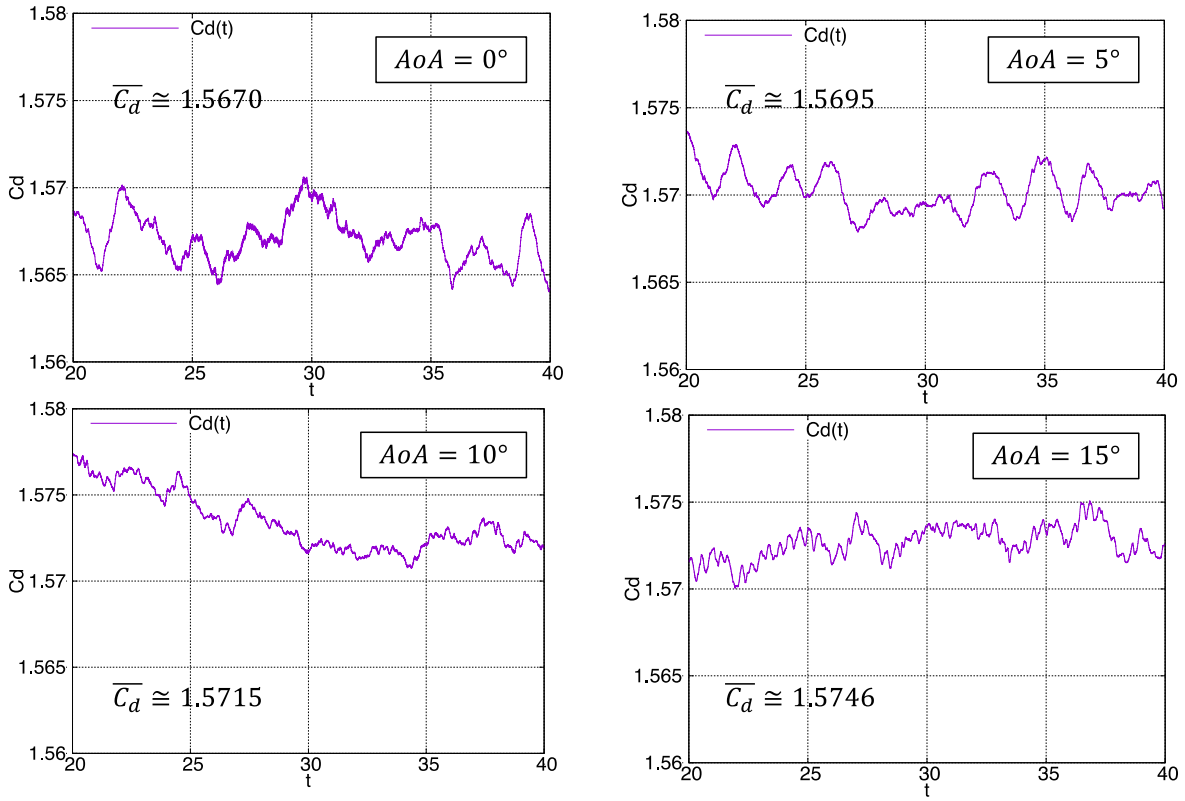

Figure 3.12: temporal evolutions of drag coefficient for different angles of attack: $Ma_\infty = 2$, $Re_\infty = 10^6$.

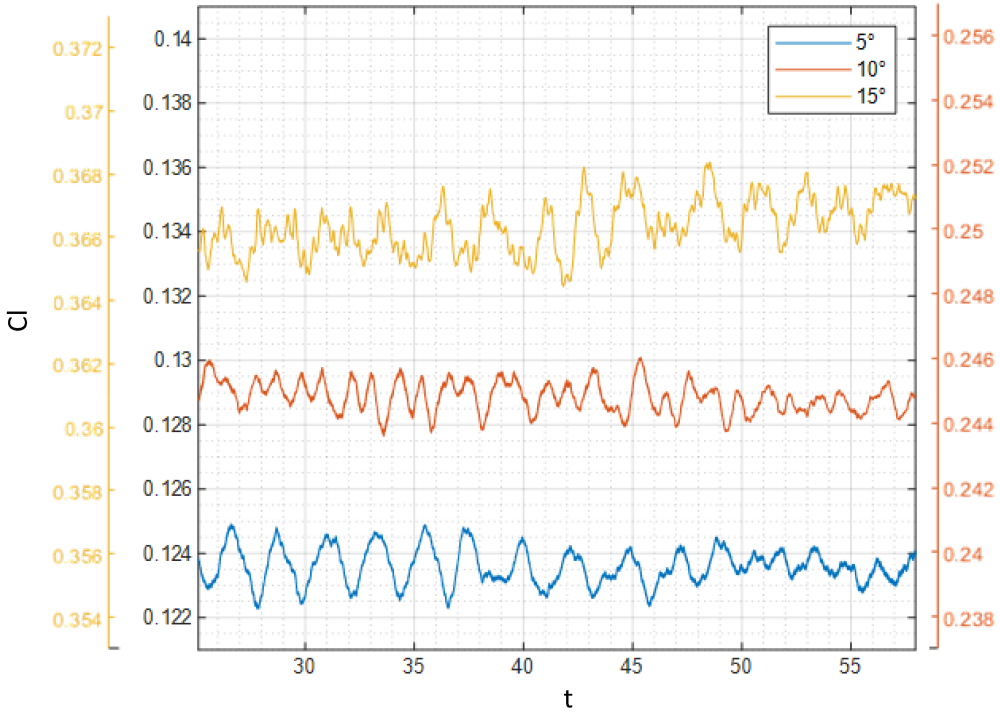

Figure 3.13: temporal evolutions of lift coefficient for different angles of attack: $Ma_\infty = 2$, $Re_\infty = 10^6$. The $AoA = 0°$ case isn't reported because the flow field is symmetrical, and the lift coefficient fluctuates around the zero.

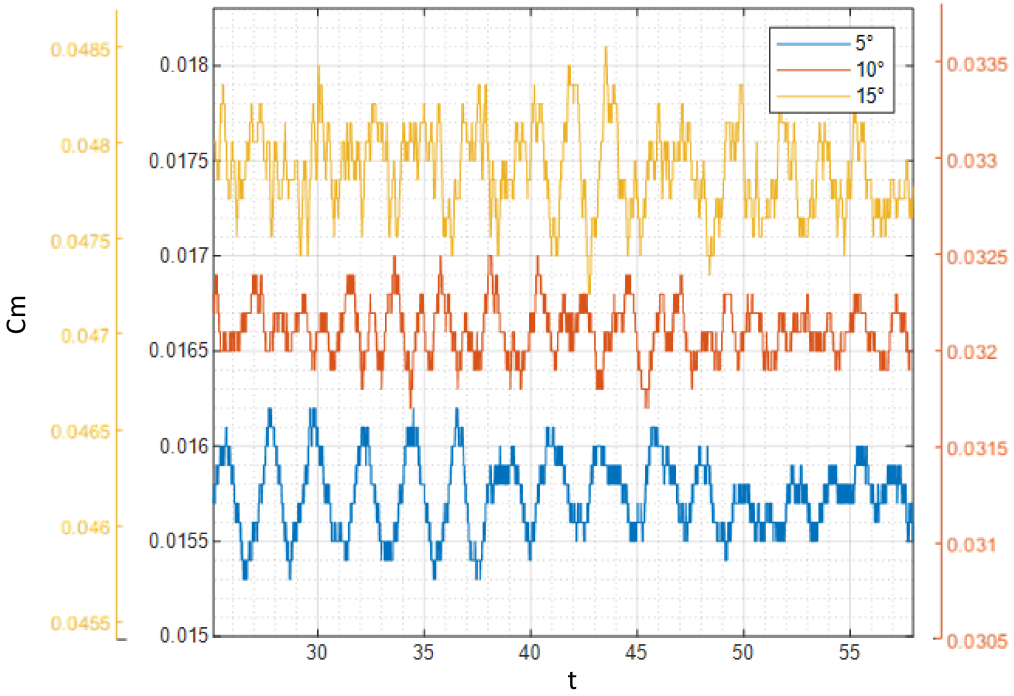

Figure 3.14: temporal evolutions of moment coefficient for different angles of attack: $Ma_\infty = 2$, $Re_\infty = 10^6$. The $AoA = 0°$ case isn't reported because the flow field is symmetrical, and the lift coefficient fluctuates around the zero.

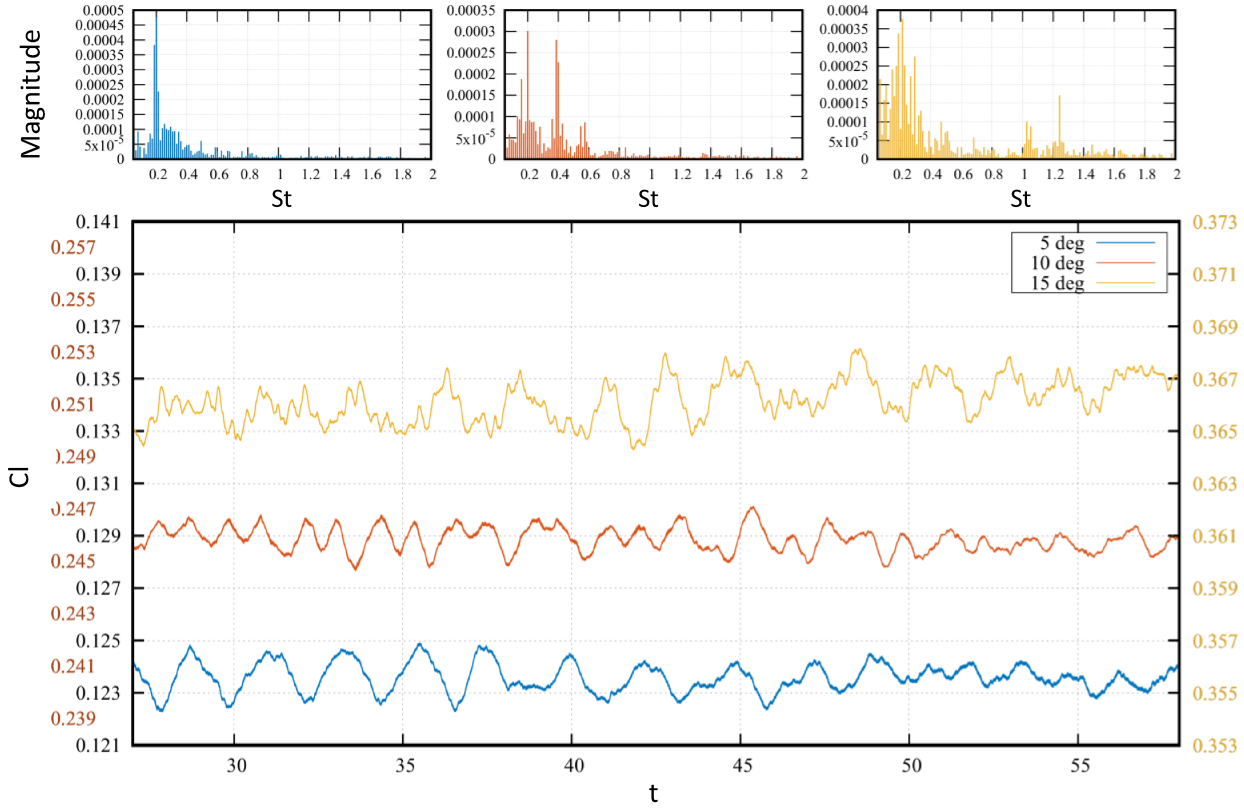

Figure 3.15: Fourier analysis of the temporal evolution of lift coefficient for different angles of attack.

1.3 Wake profiles

The wake trailing influence is visualized through wake properties profiles at different longitudinal locations. Dynamic pressure (shown in figure 3.16) and streamwise velocity (shown in figure 3.17) profiles are calculated with respect to the undisturbed values, q_0 and U_0 respectively. Dynamic pressure profiles traced for $AoA = 0°$ show the wider deficit with respect to the undisturbed value (a dynamic pressure reduction of about 90% the location $x/D = 1.5$). Such a deficit is faded for a progressive trailing distance, reaching a reduction of about 30% at the location $x/D = 8.4$. Dynamic pressure deficit exhibits a fading and a decentralization for an increasing angle of attack. Streamwise velocity profiles exhibit a negative component near the capsule highlighting the near wake recirculation region. It can be observed that the recirculation region become shorter for an increasing angle of attack, as shown by the two-dimensional contours of temperature, density, and Mach number (figures 3.3, 3.4, 3.5, 3.6, 3.8).

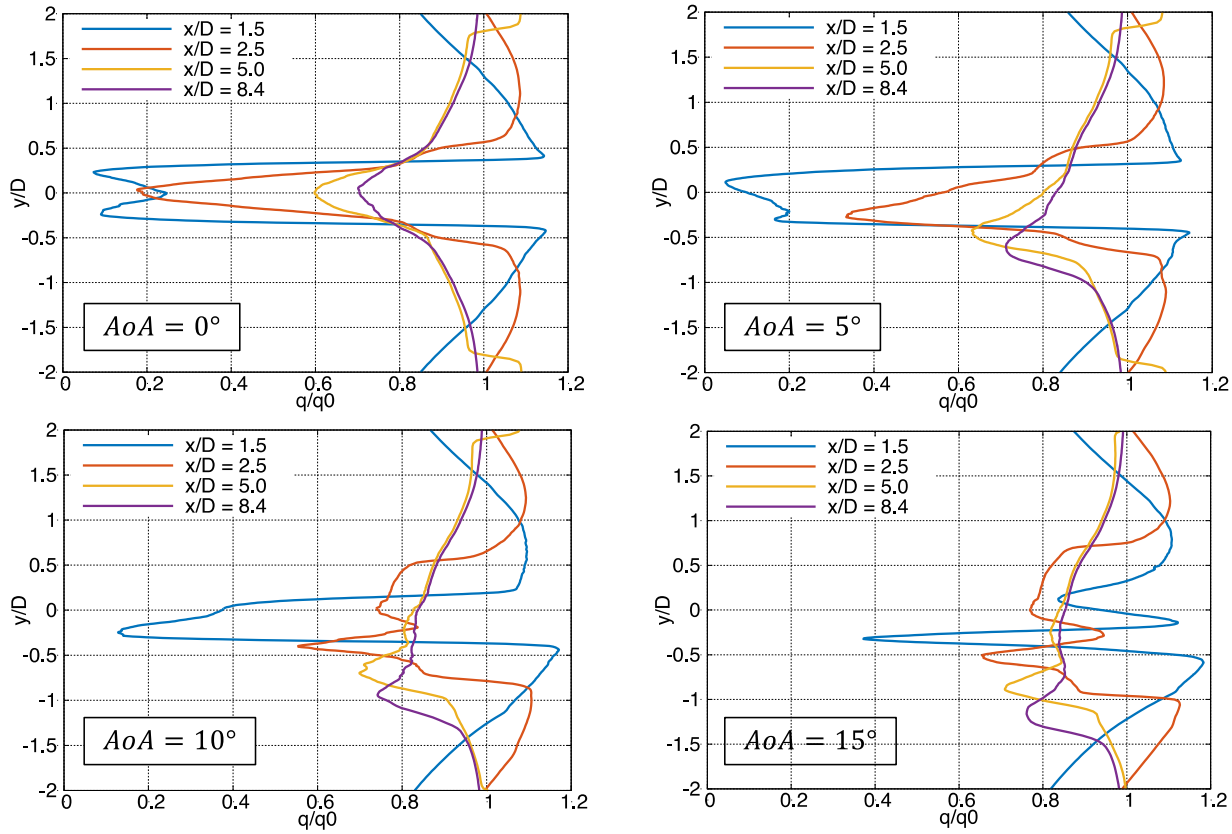

Figure 3.16: dynamic pressure profiles at different trailing distances for different angles of attack: $Ma_\infty = 2, Re_\infty = 10^6$.

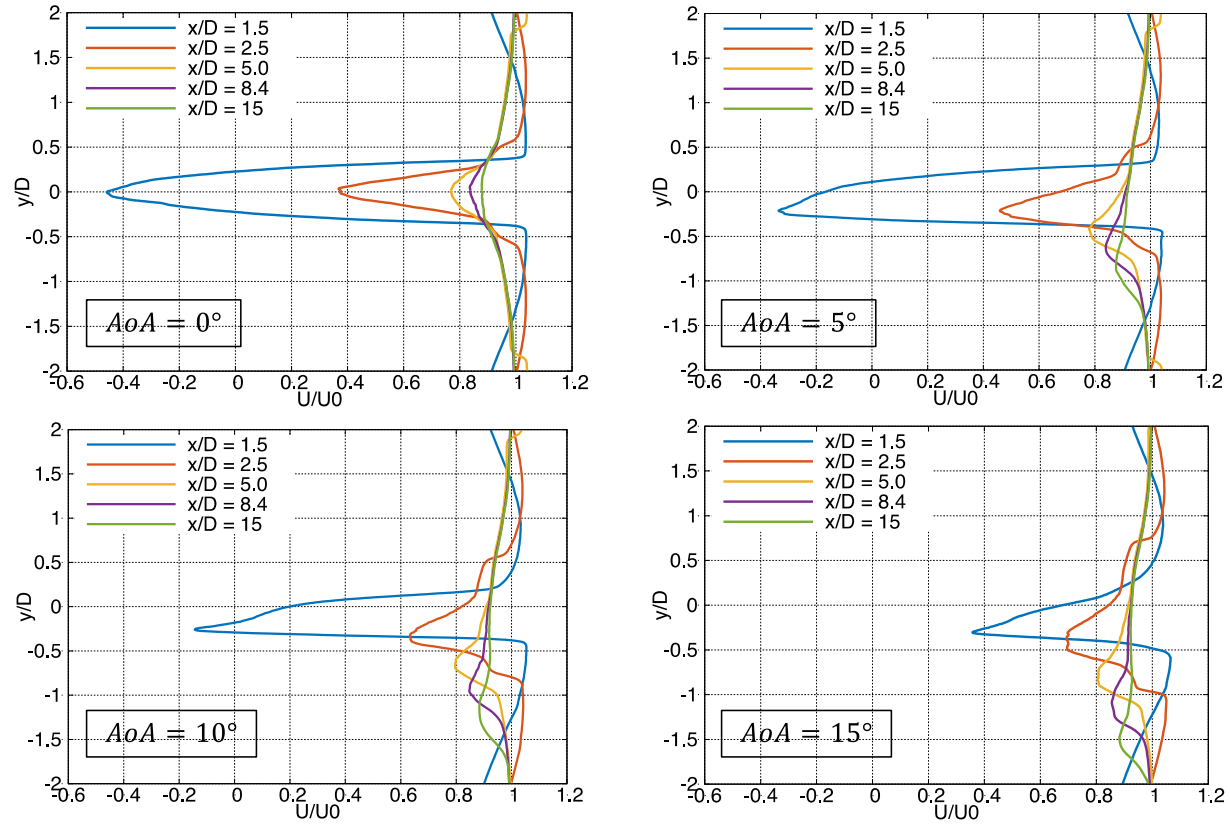

Figure 3.17: streamwise velocity profiles at different trailing distances for different angles of attack: $Ma_\infty = 2, Re_\infty = 10^6$.

Dynamic pressure profiles at different longitudinal locations in the wake of our ExoMars capsule model are compared with experimental data. Data derive from an experimental investigation of the wake properties for a Viking '75 entry vehicle model [30].

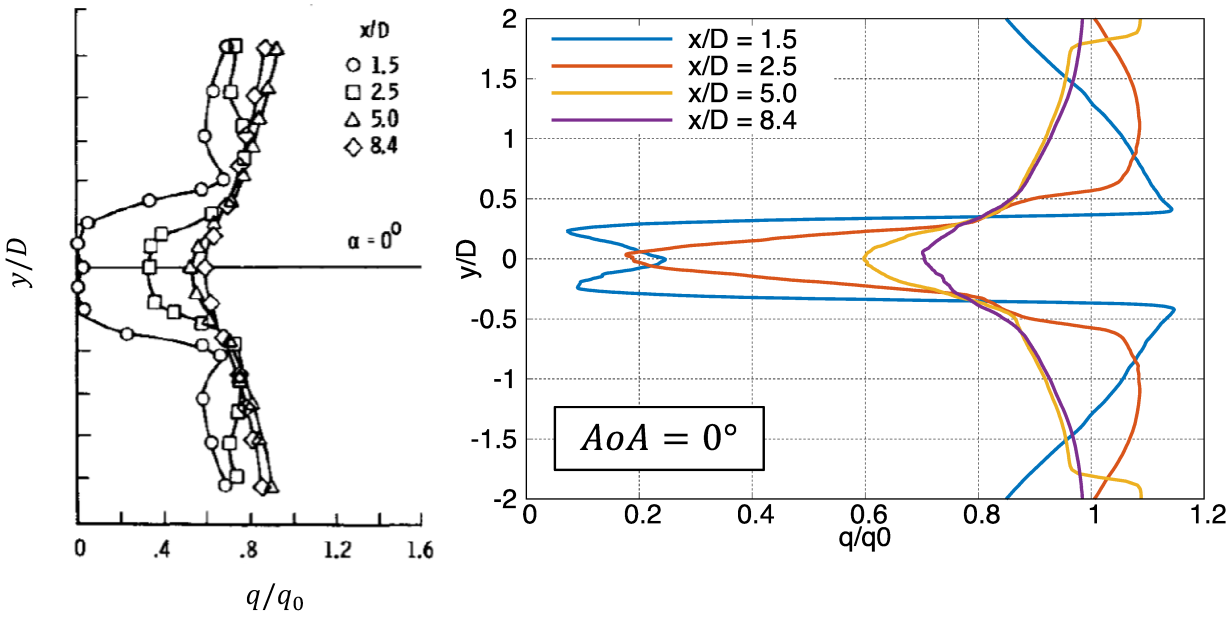

figure 3.19: dynamic pressure profiles at different longitudinal locations in the wake of ExoMars capsule model, comparison with experimental data obtained for $Ma = 2.3$ [30].

CHAPTER 4

CONCLUSIONS

In this work we performed numerical simulations to reproduce the time-evolution development of the wake produced by the ExoMars capsule during the descent phase of the EDL sequence on Mars. We referred to the ExoMars 2016 failed mission [4] to observe the aerodynamical phenomena occurring in the part of the sequence wich the parachute is intended to be deployed. Simulation setting parameters ($Ma_\infty = 2$ and $Re_\infty = 10^6$) were deduced by ExoMars AMELIA investigation of Mars' atmosphere [31]. To obtain a precise reconstruction of the turbulent wake we followed the implicit LES approach wich allows the treatment of high Reynolds flows. To cope the high computational cost involved, remarkably less than a DNS but still significant if compared to a RANS, we launched the simulations on CINECA MARCONI100 cluster. A complete simulation required from 5 to 10 days of computing. Launching and postprocessing of the results both took place remotely through Fortran 90 codes. The solver employed to perform the simulations is STREAmS [18], a high-fidelity solver validated on three types of canonical compressible flows (supersonic plane channel flow, supersonic boundary layer, shock wave/boundary layer interaction) wich exhibited high accuracy on an IBM module featuring about 10^9 nodes. STREAmS makes use of a hybrid energy-preserving/shock-capturing scheme in locally conservative form. WENO reconstructions implemented on STREAmS allows to capture shocks but maintaining a high order centered scheme in the rest of the field. This turned out to be an optimal strategy to treat the flow field around the supersonic capsule characterized by shock discontinuities and turbulent regions. Simulations have been successful and showed the wake behavior and properties for different angles of attack investigated: $0°$, $5°$, $10°$ and $15°$. Two-dimensional contours of flow field variables highlighted the wake flow changing configuration for the different angles of attack wich have been analyzed. Indeed, capsule stability and wake trailing influence were evaluated through temporal evolutions of aerodynamic coefficients and wake properties profiles at different trailing distances, respectively. Main findings regarded:

- Wake deflecting path.
- Turbulent fluctuations concentration regions.
- Bow shock and recompression shock oscillating behaviors.

- Flow field principal oscillation frequencies.

- Wake trailing distance of influence.

Results demonstrated the validity of the methodology wich has been implemented. The numerical procedure followed in carrying out this work revealed optimal for reproducing the flight conditions occurring for entry capsules. Results that have been achieved do not complete the comprehension of the aerodynamical phenomena wich manifest around a capsule-canopy system but can support further studies (different Mach conditions, simulations of the capsule coupled to a canopy, etc.) regarding ExoMars EDL sequence.

References

[1] European Space Agency. (2020, March 12). *The ExoMars Programme 2016-2022*. Retrieved from https://exploration.esa.int/web/mars/-/46048-programme-overview

[2] European Space Agency. (2020, March 12). *ExoMars Trace Gas Orbiter (TGO)*. Retrieved from https://exploration.esa.int/web/mars/-/46475-trace-gas-orbiter

[3] European Space Agency. (2020, March 12). *Schiaparelli: The ExoMars Entry, Descent and Landing Demonstrator Module*. Retrieved from https://exploration.esa.int/web/mars/-/47852-entry-descent-and-landing-demonstrator-module

[4] Toni Tolker-Nielsen, ESA IG. "EXOMARS 2016 – Schiaparelli Anomaly Inquiry". ESA, 2017.

[5] Xue, Xiaopeng and Chih-Yung Wen. "Review of unsteady aerodynamics of supersonic parachutes". Progress in Aerospace Sciences 125 (2021): 100728.

[6] Meyer, R. A. "Wind Tunnel Investigation of Conventional Types of Parachute Canopies in Supersonic Flow". COOK RESEARCH LABS SKOKIE IL, 1958.

[7] Maynard, J.D. "Aerodynamic characteristics of parachutes at Mach number from 1.6 to 3". NASA Technical Note, NASA, Washington D.C. (1961).

[8] Karagiozis, K., et al. "A computational study of supersonic disk-gap-band parachutes using Large-Eddy Simulation coupled to a structural membrane". *Journal of Fluids and Structures* 27.2 (2011): 175-192.

[9] Hinman, W. Schuyler, and Craig T. Johansen. "Mechanisms in the hypersonic laminar near wake of a blunt body." *Journal of Fluid Mechanics* 839 (2018): 33-75.

[10] H. Nakamura, K. Manabe, M. Nishio. "Flow Patterns around the MESUR Capsule Traveling at Supersonic/Hypersonic Speeds". JSME International Journal (2006), Series B, Vol. 49, No. 2, pp. 384-392.

[11] Stephen B Pope. Turbulent flows. 2001.

[12] Francisco, G., and C. R. Santos. "Transition to turbulence in the Reynolds' experiment." *Physica A: Statistical Mechanics and its Applications* 297.1-2 (2001): 73-78.

[13] Lewis Fry Richardson. Weather prediction by numerical process. Cambridge university press, 2007.

[14] Andrey Nikolaevich Kolmogorov. "The local structure of turbulence in incompressible viscous fluid for very large Reynolds numbers". In: Cr Acad. Sci. URSS 30 (1941), pp. 301–305.

[15] John David Anderson Jr. *Fundamentals of Aerodynamics*. Tata McGraw-Hill Education, 2010.

[16] Patrick Gallais. *Atmospheric Re-entry Vehicle Mechanics*. Springer, 2007.

[17] Shapovalov, V.M. On the Applicability of the Ostwald–De Waele Model in Solving Applied Problems. *J Eng Phys Thermophy* 90, 1213–1218 (2017).

[18] Bernardini, Matteo, et al. "STREAmS: A high-fidelity accelerated solver for direct numerical simulation of compressible turbulent flows." *Computer Physics Communications* 263 (2021): 107906.

[19] Boussinesq, Joseph. *Thōrie analytique de la chaleur mise en harmonie avec la thermodynamique et avec la thōrie mcānique de la lumi_re: Refroidissement et cḥauffement par rayonnement, conductibilit ̄des tiges, lames et masses cristallines, courants de convection, thōrie mcānique de la lumi_re. 1903. xxxii, 625,[1] p.* Vol. 2. Gauthier-Villars, 1903.

[20] Garnier, Eric, Nikolaus Adams, and Pierre Sagaut. *Large eddy simulation for compressible flows.* Springer Science & Business Media, 2009.

[21] Smagorinsky, Joseph. "General circulation experiments with the primitive equations: I. The basic experiment." *Monthly weather review* 91.3 (1963): 99-164.

[22] Franck Nicoud and Fr ́ed ́eric Ducros. “Subgrid-scale stress modelling based on the square of the velocity gradient tensor”. In: Flow, turbulence and Combustion 62.3 (1999), pp. 183–200.

[23] Aspden, Andrew, et al. "Analysis of implicit LES methods." *Communications in Applied Mathematics and Computational Science* 3.1 (2009): 103-126.

[24] Bernardini, M., et al. "Large-Eddy Simulation of Vortex Shedding and Pressure Oscillations in Solid Rocket Motors." *AIAA Journal* 58.12 (2020): 5191-5201.

[25] Peskin, Charles S. "The immersed boundary method." *Acta numerica* 11 (2002): 479-517.

[26] Mittal, Rajat, and Gianluca Iaccarino. "Immersed boundary methods." *Annu. Rev. Fluid Mech.* 37 (2005): 239-261.

[27] Uhlmann, Markus. "An immersed boundary method with direct forcing for the simulation of particulate flows." *Journal of Computational Physics* 209.2 (2005): 448-476.

[28] Breugem, Wim-Paul. "A second-order accurate immersed boundary method for fully resolved simulations of particle-laden flows." *Journal of Computational Physics* 231.13 (2012): 4469-4498.

[29] Boukharfane, Radouan, et al. "A combined ghost-point-forcing/direct-forcing immersed boundary method (IBM) for compressible flow simulations." *Computers & Fluids* 162 (2018): 91-112.

[30] Campbell, James F., and Clarence A. Brown Jr. "Experimental Wake Flow Properties of a Viking'75 Entry Vehicle." *Journal of Spacecraft and Rockets* 11.1 (1974): 11-15.

[31] Ferri, Francesca, et al. "Exomars atmospheric mars entry and landing investigations and analysis (amelia)." *Space Science Reviews* 215.1 (2019): 1-21.